UNIVERSITY OF TARTU
FACULTY OF SCIENCE AND TECHNOLOGY
Institute of Chemistry

Pavle Ramah

Synthesis, characterisation, and analysis of the time degradation of lithium alanate/carbon black composites

Master's thesis (30 ECTS)

Materials Science and Technology

Supervisor: Rasmus Palm, PhD

Kenneth Tuul, MSc.

Tartu, 2022

ABSTRACT

Synthesis, characterisation, and analysis of the time degradation of lithium alanate/carbon black composites

Solid-state hydrogen storage is slated to play a significant part in the development of thhydrogen economy. Lithium aluminium hydride ($LiAlH_4$) is one such material - a metal hydride with a high gravimetric content of hydrogen. Its thermodynamic and kinetic properties have been researched in depth, with the goal of improving its cyclability and desorption kinetics. A way to improve these properties is to nanostructure the material within a porous host. In this master's thesis, composites of varying wt% of $LiAlH_4$ were synthesised with commercially available carbon black (Vulcan XC72R) via ball milling. The prepared composites were then characterised (temperature-programmed dehydrogenation, X-ray diffraction, gas sorption), where particular attention was paid to the improvement of H_2 release properties. Additionally, time-stability of the hydrogen storage properties under ambient storage conditions was investigated.

Keywords: solid-state hydrogen storage, complex metal hydrides, carbon black, ball milling

CERCS code: P400 Physical chemistry, T140 Energy research, T150 Material technology

Liitiumalanaat/süsiniktahm komposiitide süntees, karakteriseerimine, ning aja-stabiilsuse analüüs

Tahke-faas vesiniku salvestusel on tähtis roll vesiniku-põhise majanduse arendamisel. Liitiumalumiiniumhüdriid (LiAlH4) on potentsiaalne tahke-faas metallhüdriid vesiniku salvestuseks, omades kõrgetd gravimeetrilist vesiniku sisaldust. Antud materjali vesniku hoiustamise termodünaamilisied ja kineetilisied omadusi on uuritud põhjalikult, eesmärgiga parandada materjali tsükleeritavust ning vesiniku vabastamise kineetikat. Üks võimalus vastavate omaduste parandamiseks on nanostruktureerimine poorses kandematerjalis. Antud magistritöös sünteesiti kuuljahvatamise meetodiga erineva mass%-ga LiAlH4 komposiidid kommertsiaalselt kättesaadava süsiniktahmaga (Vulcan XC72R). Valmimstatud komposiidid karakteriseeriti temperatuur-programmeeritud dehüdrogeenimise, röntgendifraktsiooni ja gaasi sorptsiooni meetoditega....., kus erilist tähelepanu panti osutati vesiniku eraldumise omaduste parandamisele. Lisaks eelnevale uuriti hoiustus-aja mõju komposiitmaterjalide vesiniku hoiustamise omadustele.

Table of Contents

INTRODUCTION

The significance of pursuing new alternatives to traditional fossil fuel energy sources cannot be understated. The state of the environment, after all, is the predominant topic of modern discourse for a reason – a recent report from The Sixth Assessment Report (AR6) of the United Nations (UN) Intergovernmental Panel on Climate Change (IPCC) shows alarming trends of climate change [1]. To address this problem means to work towards a new energy system consisting of renewable energy sources and the corresponding mediums that allow their storage and usage.

Hydrogen is one of the prime candidates as a sustainable and renewable energy carrier, and it is a particularly interesting compound for *storing* energy. Hydrogen is considered a viable energy carrier due to the inevitable decrease of oil supply, geo-political factors, and a need for a sustainable and greenhouse gas emission-free solution that can be used in a variety of industries and many kinds of applications. The ultimate goal of using hydrogen is to diversify societies' energy profiles, aiming to, eventually, and in combination with other energy sources (e.g. other renewables like wind or solar power, nuclear power), fully replace polluting, non-renewable resources [2].

Hydrogen is most commonly synthesised in two ways: through the electrolysis of water, or steam reforming. The electrolysis of water, which in itself is abundant but might require pre-processing, e.g. desalination, is a carbon-neutral route of synthesis. Steam reforming meanwhile uses hydrocarbons as precursor materials and emits significant amounts of carbon dioxide [3].

This thesis will not delve deeply into the sustainability and details of the hydrogen economy[1], but its worthwhile to address the difference between the so-called green and grey hydrogen[2], in respect of how they are procured. Green hydrogen refers to a truly renewable (in all but technicalities) source of hydrogen – electrolysis of water. Electrolysis of water is a process in which (pure) water is decomposed into oxygen and hydrogen gas, by expending electrical energy at voltages higher than 1.23 V [3]. Of course, it should be noted that the source of energy inputted for electrolysis is an important factor when it comes to calling electrolysis green. Green hydrogen is defined when the electrolysis is powered by a renewable primary source – like wind or solar power [4]. Meanwhile, grey hydrogen is hydrogen procured from natural gas, a notoriously dirty and expendable source, through the process of steam reforming which as a side-product generates large amounts of carbon dioxide [3].

Hydrogen can be used as a fuel with high efficiency, for example, when used in polymer electrolyte membrane (PEM) fuel cells [8]. This paves the way for a specific type of energetic restructuring, something that is frequently referred to as the hydrogen economy. The hydrogen

[1] For an interesting overview and modelling, one should refer to [5] and [6]

[2] Note: the apparent colour spectrum of hydrogen differs somewhat depending on the source and other factors – frequent are mentions of blue, black, pink, white, or even brown hydrogen – for the sake of clarity and in line with the referencing, this thesis will stop at a broad, general dichromatic categorisation. For more detail, one could refer to [7].

economy is a broader term than just an energetic restructuring model – the hydrogen that's at the centre of it has the potential of use in not only industrial sectors (e.g. ammonia production, metallurgical industries) but also commercial and residential sectors as a fuel (e.g. gas grids and household appliances) [9].

However, the use of hydrogen as an alternative fuel has its difficulties. Two of the primary ones, especially when considering the automotive application, which is one of the focal points of research, are safety and volumetric requirements. Hydrogen, when stored as compressed hydrogen gas both has low volumetric energy density (i.e. how much energy a system contains in comparison to its volume) and possesses safety concerns (i.e. flammability, high-pressure constraints) in such a device. Due to this, research has steered into finding alternative ways of storing hydrogen to circumvent these faults. One possibility is liquid hydrogen – but due to low-temperature demands, it doesn't meet the on-board application requirements in the automotive industry [9].

Metal hydrides, carrying the hydrogen chemically bound inside a molecule (or, in the case of interstitial metal hydrides, a metal crystal lattice), provide the possibility of high volumetric densities, along with a perspective towards long-term stability. The general downsides of such a solution are irreversibility, high temperatures required for hydrogen release, and its low gravimetric densities (how much energy a system contains per a unit of its mass), which mostly do not meet the US Department of Energy (DoE) hydrogen storage material expectations [10]. These demands are even further increased by the European VII FP call [11]. It should be noted that particular hydrides might have other specific downsides.

In the case of lithium alanate ($LiAlH_4$), a particular type of complex metal hydride, hydrogen makes up approximately 10.6 wt% of the material, which nominally fully meets the DoE requirements in terms of capacity. Still, the applicability of $LiAlH_4$ is limited by its kinetic and thermodynamic factors, as well as practical factors (only 7.9 wt% of hydrogen capacity is usable under the operational conditions of current fuel cells) making lithium alanate hard to efficiently use and inhibiting cyclability [12].

Lithium alanate as a hydrogen storage material is the principal topic of this thesis. Composites with carbon black were synthesised via ball milling in a variety of compositions (from 20 wt% to 80 wt% alanate, in increments of 10 wt%) and characterised in detail, including investigating its time-dependent degradation. A change in dehydrogenation behaviour and a significant reduction in on-set dehydrogenation temperature is shown.

Finally, this introduction concludes with a note: the use of hydrogen as a focal part of a new energy system, while not without faults and constraints, may pave a new direction for our future relationship with the planet we live on. With future improvements and a thorough consideration of its sourcing (i.e. grey versus green) there is no reason to believe it cannot become optimal.

1. Literature overview

1. 1. Hydrogen storage materials

For use as energy carriers, hydrogen storage materials should possess the following properties [13]:

- favourable thermodynamic properties (e.g. adequate adsorption/desorption temperatures and enthalpy of (de)hydrogenation),
- fast kinetics (e.g. rapid (de)hydrogenation),
- cyclability (e.g. number of hydrogenation – dehydrogenation cycles without a significant loss of capacity),
- high volumetric and gravimetric energy density,
- sustainable (e.g. environmentally friendly production, abundance of raw components, recyclability)
- and economic viability.

Hydrogen can be stored in the following aggregative states: gaseous, liquid, or solid.

If stored as a gas, hydrogen is compressed inside high-pressure tanks. In of itself, the process of pressurization causes significant reduction in actual system efficiency due to the energy required to compress it. The US Department of Energy (DoE) data for the energy required for H_2 compression from atmospheric pressure to 350 and 700 bar from on-site H_2 production is approximated as 1.7 and 6.4 kWh/kg$_{H_2}$, respectively [14]. This by itself holds plenty of limitations to any on-board application – the tanks need to be durable enough to withstand the stresses that occur during possible extraordinary situations while driving (e.g. accidents, temperature extremes). To adapt these high-pressure tanks to align with rigorous safety standards then might cause considerable cost increases. In addition, gaseous hydrogen has a low volumetric density.

If stored as a liquid, it is kept under low temperatures in cryogenic tanks, with the temperatures required being around 20 K. It has higher volumetric densities than its gaseous counterpart, but requires significant efforts to liquefy it, rendering it similarly impractical. Liquefaction energy requirements, while cooling down from ambient conditions, are substantially higher than its gaseous counterpart, typically 10 kWh/kg$_{H_2}$ or 13 kWh/kg$_{H_2}$, if the industry standard conversion of ortho- to para- liquid H_2 is accounted for [9, 14].

It's useful to note that compression energy requirements range approximately in 5 - 20% of the lower heating value (LHV)[3] of hydrogen (33.3 kWh/kg$_{H_2}$), while the liquefaction process ranges within 30 - 40% of the LHV. Theoretical energy requirements for both the compression to 700 bar and the liquefaction to 20 K are significantly lower than those of currently available methods, and range within 4 - 10% of LHV respectively [14]. This indicates that while 100%

[3] Lower heating value (LHV) is a measure of available thermal energy produced by a combustion (rapid reaction with oxygen) of a fuel, from ambient conditions until the return of temperature to 150 °C (as opposed to higher heating value which presumes return to ambient, which becomes significant for the water byproduct since the heat of vaporisation becomes recovered), measured as a unit of energy per mass of the substance.

efficiency and achieving of theoretical values will never be possible, significant improvements still might be.

Finally, as a solid, it is chemically or physically bound within other molecules, like metal hydrides or nanostructured materials. Nanostructured materials (e.g. carbon nanotubes) can store hydrogen mostly through physical processes, the amount of which is closely related to the porosity of the nanostructure, i.e. its specific surface area (ratio of surface area to mass). The major flaws of these materials are their low volumetric and gravimetric energy densities. Metallic hydrides meanwhile store hydrogen chemically within more complex molecules. The hydrogen "tied" in both of these ways can be released by affecting temperature, pressure, or other conditions. This process is closely related to the material's crystal structure [15, 16].

Generally, we can group metallic hydrides into intermetallic and complex hydrides. Intermetallic compounds are defined as solid phases involving two or more metallic or semi-metallic elements with an ordered structure and often a well-defined and fixed stoichiometry [17]. Intermetallic hydrides form through a multi-step process in which molecular hydrogen is physisorbed through intermolecular forces at the adsorbent surface – this is followed by the reduction of a possibly pre-existing passivated oxide layer by hydrogen and successive dissociation of hydrogen into its atomic form (H_2 to H). This is followed by chemisorption, i.e. a chemical change with the formation of a mono-layer hydride, characterised by the H^- chemical species. The H^- developed in this process then proceeds to diffuse towards the bulk material, where it is "captured" by the larger voids of a metallic crystal lattice [18]. Intermetallic hydrides generally possess low gravimetric capacities [16, 19].

Meanwhile, complex metal hydrides bind hydrogen molecularly, with a clear chemical and structural change, accompanied by higher values of reaction enthalpies. Complex metal hydrides consist of a metallic cation and a hydrogen-bearing anion complex. This contrasts with the interstitial hydrogen situated between metal atoms (i.e. the hydride in the vacancies of the larger crystal structure) in intermetallic hydrides, leading them to be largely dependent on their crystal structures [16, 18]. The hydrogen release mechanism is significantly more complicated compared to its intermetallic analogue and remains not fully explained [20]. In Table 1, some gravimetric and volumetric capacities of metal hydrides are given, along with the DoE requirements and the gas and liquid storing methods [21, 10].

Table 1. Gravimetric and volumetric densities of some hydrogen storage materials[4], along with DoE goals

Type	Gravimetric density, H_2 wt%	Volumetric density, kg H_2/m^3
$LiAlH_4$	10.6	90
$NaAlH_4$	7.4	88
LiH	12.7	95
pressurised H_2 (g)	100	<50
H_2 (l)	100	72
DoE goal	6.5	>50

[4] Note: the actual values would likely be somewhat lower, when incorporated in an actual hydrogen storage system

1.1.1. Complex metal hydrides

Complex metal hydrides consist of metal cations (e.g. Mg, Li, Na) and polyatomic hydrogen-bearing anions, such as amides, borohydrides, and alanates. Hydrogen in these compounds is covalently bound to the anionic carrier (in amides (NH_2^-), nitrogen; in borohydrides (BH_4^-), boron; in alanates (AlH_4^-), aluminium). All of these elements are light, which is reflected in their high gravimetric H_2 content (Table 1) and low densities (on the low-end for $LiBH_4$ at 0.66 g/cm^3 to the high-end of KNH_2 at 1.57 g/cm^3) [22, 21].

Complex metal hydrides have reached the spotlight of current solid-state hydrogen storage research after a series of papers by Bogdanović et al. [23, 24] changed the scientific perception of them. Complex metal hydrides were previously considered as, while always theoretically gravimetrically capable, ultimately unsuitable for real world applications due to relatively sluggish kinetics, unsuitable thermodynamics (i.e. high stability) and inferior or outright impossible cyclability. Bogdanović et al. achieved significantly improved properties by using titanium dopants on lithium and sodium alanate systems. This paved the way for an intense increase in research into metal hydrides as vehicles for hydrogen storage (Figure 1). [25].

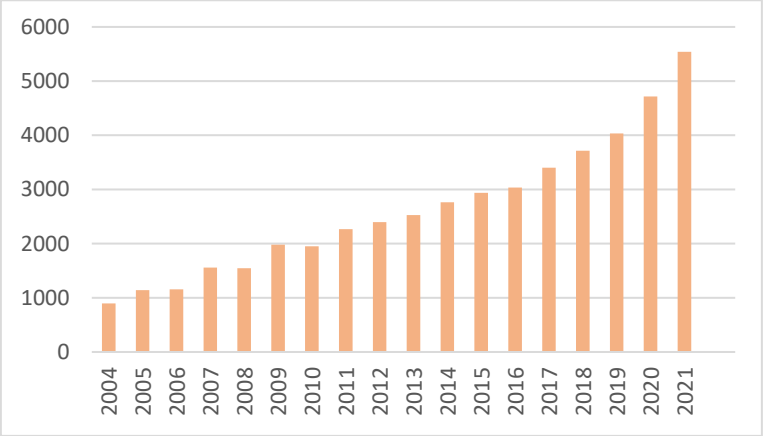

Figure 1. Graphic representation of published articles per year as sourced from Dimensions.ai, with keywords „metal hydrides“ and „energy storage“, limited on chemical sciences, physical chemistry, and materials engineering journals

The general high hydrogen storage capacities of complex metal hydrides make them ideal for use as solid-state hydrogen storage compounds. Where Bogdanović’s research mostly dealt with Ti-based catalysts, there have been recent indications of other effects that influence a hydride’s properties for the better – one of which is the nanoconfinement of the hydride, which leads to significant thermodynamic destabilization and improved kinetics [26].

1.1.2. Lithium alanate

Lithium aluminium hydride – or lithium alanate – is a complex metal hydride that can be thought of as consisting of a Li^+ cation and an AlH_4^- anion. It has long been considered a candidate for solid-state hydrogen storage. It has a high hydrogen capacity of 10.6 wt% as exhibited in its three dehydrogenation reactions (Table 2).

Table 2. Degradation reactions of lithium alanate, their enthalpies [27, 28], and on-set dehydrogenation temperatures [29]

no.	reaction	ΔH_r[5], kJ/mol	T_{onset}, °C
R1	$3LiAlH_4 \longrightarrow Li_3AlH_6 + 2Al + 3H_2\,(g)$	3.5	≥ 140
R2	$Li_3AlH_6 \longrightarrow 3LiH + Al + 3/2H_2\,(g)$	14.5	≥ 180
R3	$3LiH + 3Al \longrightarrow 3LiAl + 3/2H_2\,(g)$	140	≥ 400

The first step of this sum-reaction happens at temperatures higher than 140 °C under normal conditions. However, some researchers postulated that it is in fact a combination of two steps – a phase transformation to melt $LiAlH_4$ at 165 - 175 °C (being an endothermic process), before decomposing and exothermically recrystallising to form the hexahydride [29].

The second step occurs during an endothermic melt reaction in the range of 180 - 220 °C to form lithium hydride.

However, the third reaction happens at such high temperatures and requires intense energies as to be considered irrelevant for most if not all H_2 storage applications. Hence the usable hydrogen capacity, the one that fits the first two steps, is 7.9 wt% (first step 5.3 wt%, second step 2.6 wt%). The release of H_2 in these three steps of lithium alanate degradation is instrumentally recorded and presented in the following figures, where Figure 2a shows the differential release of H_2 and Figure 2b the cumulative release of H_2.

[5] There exist certain discrepancies when it comes to enthalpy values of the step reactions of the decomposition of lithium alanate. For example, Ares et al. [29] note that the enthalpy of the first step is very dependent on the heating rate – at rates higher than 1 °C/min the reaction becomes exothermic, as high as -14 kJ/mol (attributing it to melting processes), while at lower heating rates it is endothermic and equal to 1.6 kJ/mol. Meanwhile, Løvvik et al. [27] calculate this value through DFT simulations to be 9.8 kJ/mol, rendering the step endothermic, and compare it to previously known experimental data of 3.5 kJ/mol. It is this value that is used in this table.

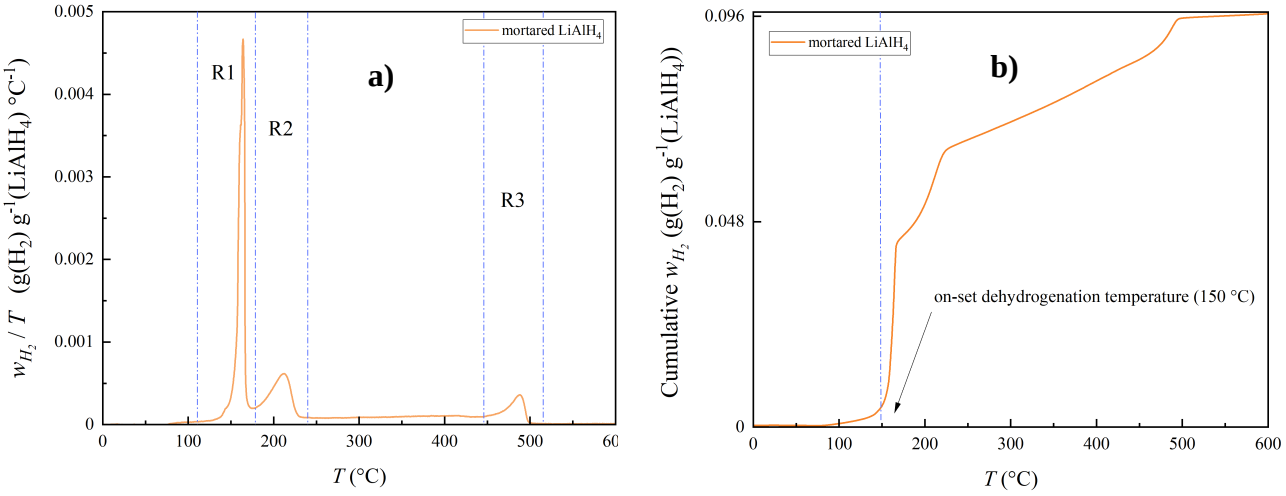

Figure 2. The a) differential and b) cumulative release of H_2 in mortared lithium alanate. The ramp rate used was 2 °C/min. R1, R2, R3 correspond to the reaction steps as described in Table 2. The on-set dehydrogenation temperature is clear and can be read as 150 °C.

All three reaction steps are dependent on the heating rate, indicating that the crystallinity changes dominate the process [29]. Some discrepancies regarding the postulated steps have been recorded and further investigation into the nature of these reaction steps seems necessary [30]. Despite rather detailed research into the thermodynamic behaviour of the system, doubts remain to the exact decomposition process route based on the beforementioned discrepancies [31, 32].

More interestingly, the thermodynamics of this process leave more questions than they answer. All three degradation steps are nominally endothermic, but with such low enthalpy values[6] for the first two reaction steps compared to the third one leads researchers to conclude that, in normal conditions, lithium alanate is a metastable compound [33]. This metastability is driven by the entropy effects and most likely stems from lattice instabilities (starting from temperatures as low as 100 K), a precursor phenomenon for decomposition. These instabilities are related to the binding of the complex anion, which causes lithium alanate to have a very slow, but steady natural decomposition rate to its hexahydride form [35]. However, the decomposition rate is very slow, the half-life being at about 20 years or so in storage. In the presence of impurities, the rate of natural decomposition increases drastically [27].

Jang et al. investigated the equilibrium behaviour of pure lithium alanate to determine whether a rehydrogenation reaction would be possible under practical temperature and pressure ranges. They determined that 10^3 bar of hydrogen partial pressure would be required to induce the reverse reaction of Li_3AlH_6 to $LiAlH_4$, rendering it impossible under practical conditions [36].

[6] Simulation experiments determined that while the enthalpy for the second step of degradation coincides with simulated data very well, the first steps shows marginally higher values of 9.8 kJ/mol. The root cause of these discrepancies has not been determined. [34]

It is then needed to induce a change in the thermodynamic properties of the material to bring about this reversibility. This will be explored in the following sections of this thesis.

There are several approaches to the synthesis of lithium alanate. The most prominent one is the physiochemical pathway of "direct" synthesis from LiH and Al, in the presence of hydrogen gas and an organic solvent like tetrahydrofuran (THF) or dimethyl ether. After the creation of a $LiAlH_4 \times 4$ THF adduct, pure lithium alanate is recrystallised and dried from excess THF. This is a notable procedure because the majority of (partially) successful rehydrogenation procedures are based on similar chemistry. A more industrially common approach is reacting LiH and $AlCl_3$, instead of pure aluminum, dispersed in an organic solvent (THF being the most common) [37, 38].

As previously described, lithium alanate can be thought of as ionically bound lithium cation and alanate anion. Within the anion, the bond between aluminium and hydrogen can be considered strictly covalent. Neutron scattering of a isotope analogue – $LiAlD_4$ – shows that the structure consists of well-separated AlD_4 tetrahedra, while the Li atoms serve as connectors. Each Li atom is bonded to one deuterium atom from each of the five surrounding AlD_4 tetrahendra, resulting in a trigonal bipyramidal coordination. The Al-D bond length (i.e. distance) is in the range of 160.3 – 163.3 pm, while the surroundings of Li show significantly less coordination, as evident by higher ranges of Li-D distances – 183.1 – 197.8 pm. It should be noted that these measurements were measured in cryogenic temperatures of 8 K. The $LiAlD_4$ structure belongs to the P21/c space group [39].

When it comes to crystal structure, lithium alanate mostly takes the so-called alpha form. The beforementioned $LiAlD_4$ was of the same form. Only under much higher pressures (above 26 000 bar) does this crystal structure transition into the beta and gamma forms, characterised by different space groups. These are irrelevant for the purposes of this thesis, considering that these pressures are very far from the ones expected for use in hydrogen storage technologies [12].

The question of the regeneration of lithium alanate is a complex one. Sodium alanate, which positioned itself as a prime candidate for the use as a hydrogen storage device, did so specifically because of its ability to be successfully and practically regenerated (while still keeping a relatively high enough H_2 capacity of 4.2 wt%, compared to the usable maximum of 5.5 wt%) through the process of rehydrogenation in the presence of a Ti-based catalyst, in the pioneering work of Bogdanović et al. This influenced the subsequent research direction, where the vast majority of literature sources that deal with the rehydrogenation of lithium alanate are using Ti-based catalysts [23].

One of the earliest synthesis methods, one presented by Ashby et al., started from the dehydrogenation products and directly synthesised $LiAlH_4$ in an organic solvent (THF). This involved high pressures of around 345 bar and temperatures of 120 °C. This served as a basis for most of the regeneration procedures that will be described here, even if the original research didn't even consider alanates as hydrogen storage materials [40].

Other more industrial approaches to synthesis of lithium alanate include the metathesis reaction (usually during ball-milling or heating) – a chemical process that includes an exchange of bonds between two reacting species. In this case, the metathesis occurs between lithium and

sodium species. A common example is a reaction between lithium borohydride and sodium alanate, resulting in lithium alanate and sodium borohydride [12]. Ashby et al. presented a similar approach as a high-yield way of obtaining lithium alanate from sodium alanate and lithium chloride [40]. In this case, it is sodium alanate that is directly synthesised from the elements.

Wang et al. presented a five step physicohemical pathway for the regeneration of $LiAlH_4$ from its dehydrogenation products. The alanate is Ti-catalysed, and the solvent in question is THF. The retrieval of alanate by this method is adequate, but the process is demanding, mostly because of the solvent and catalyst removal [37]. Same principle was used by Chen et al. [41].

Graetz et al. modified this procedure with a Ti-catalysis of Al product of dehydrogention, and used the adduct $LiAlH_4 \times 4$ THF and its subsequent desolvation to recover pure alanate. Once again, a step of THF removal is necessary [42].

A further modification of this method by Liu et al. was done by switching the solvent for the room temperature evaporable dimethyl ether, achieving a total of 64 wt% capacity recharge during cycling. Long term cycling however was not done which leaves the ultimate applicability of this method unknown. Further more, the authors noted an agglomeration of the catalyst between cycles, which required ball milling in between cycles. Along with this, the catalytic activity decreased during further cycles, leading to higher on-set temperatures of dehydrogenation over the cycles [43]. Similarly, Humprhies et al. confirmed this in an *in situ* NMR study, and indicated that the reaction occurs even at sub-ambient temperatures [44].

Here are described three variations of a same direct synthesis method described more than fifty years ago by Ashby [40]. No alternate approaches to regeneration of alanate have been successfully applied to the author's knowledge.

1.2. Nanostructuring

1.2.1. Nanoscale

A way of destabilising lithium alanate to suit application in hydrogen storage industries is nanostructuring. Nanoparticles – materials that are in the sub 100 nm range – generally possess wildly different properties compared to their bulk counterparts. Approaching the nanoscale, the changes in properties become abrupt, rather than incremental. Generally speaking, this stems from two main reasons:

a) the increase of the specific surface area, which leads to increased amount of surface atoms that are destabilised due to the relative lack of intermolecular interactions of the same species on the surface side, to the extent that the majority of particles are surface molecules. This can also increase the number of unsatisfied chemical bonds compared to bulk molecules, which leads to an increase in surface energy and impacts the reaction enthalpy. The impact on the entropy of the material might also be significant, due to the exposedness of the surface molecules. The molecules no longer burdened from bulk influence contribute to disorder, which can lead to increased reactivity [22, 26];

b) nanoscale diffusion lengths, which can lead to quantum phenomena (e.g. quantum confinement) the closer the particles get to their molecular constituents, influencing a wide variety of properties, including thermodynamic and kinetic properties. Shortened diffusion pathways sometimes can also change the rate limiting process or the whole reaction pathway for a process [22, 26]. In the case of complex hydrides, this can influence the surface processes of physisorption and chemisorption that are crucial for (de)hydrogenation, since the diffusion pathways are comparatively shorter than on a non-nano scale.

It should be noted however that nanostructuring is a general term that leaves it unclear whether nanoencapsulating or nanoscaffolding take place. Nanoencapsulating is encapsulation or coating of a material within a rigid matrix on a nanoscale. Nanoscaffolding is a formation of a nanostructured material inside a (generally porous) host [22]. This thesis will deal with nanoscaffolds as a means of improving the properties of lithium alanate by preparing a composite of it with a mesoporous, commercial carbon.

The case of complex hydrides when it comes to their nanostructuring is a complicated one. The methods of achieving nanostructures are diverse, but in practice, due to ease, availability, and practicality, they mostly come down to mechanical and chemical methods. These can be reproduced consistently to at least some extent, and don't require special and expensive methodology which would barr them from practical use in industry. However, true nanoscale can remain elusive. For example, one of the methods that will be considered here, ball milling, achieves dimensions of tens of nanometers only after extensive operation. Control over the size distribution is another challenge, as is the destruction of the material in the case of mechanistic methods [22, 45]. Despite this, the results achieved by such nanostructuring universally show one thing – an improvement in the required properties. This leads to a significant amount of uncertainty when it comes to whether true nanoscale was achieved and determining the origin of the improved properties. The evident truth then is that the properties of metal hydride nanocomposite are variables of many factors, some that begin at the microscale and become more influential as they approach the nanoscale. These include the diffusion lenghts, the morphology, the nature of interactions between the scaffold and the hydride, the amount of defective surfaces and their interfaces, among others [22, 46].

Finally, it should be noted that an universal problem with nanostructuring materials is their tendency toward agglomeration – an escape back into the macro scale. This is very case-specific, but nonetheless presents a real issue accross the board, to varying extent [47].

1.2.2. Preparation methods

When it comes to synthetic methods of nanoscaffolding, they can be divided into two sub-branches – top-down and bottom-up. It's needless to say that top-down approaches are more common and more practical. The main example could be ball milling, where particles are being ground down to nanoscale, sometimes in the presence of a catalyst or dopant. The flaws of top-down methods are general lack of controlability, heterogenity, and wide particle size distributions that in certain cases cannot reach the nanoscale. Bottom-up approaches meanwhile are more sophisticated, but also demanding and intensive on method development, while still posessing issues of heterogenity and possibility of contamination. These include gas-

phase synthesis, chemical/electrochemical reduction, and infiltration of porous materials by melts/solvents [22].

Ball milling is the principle technique of this thesis and will be described in full in the following segment. It is one of the most common techniques of reducing particle size and does it by purely mechanistic means: grinding of the material in presence of a harder, inert one with high energies (which itself is a function of ball type and weight, grinding conditions etc.). The fashion of this grinding depends on the method, but most commonly it is centrifugal force.

Gas-phase synthesis most commonly consists of vaporisation of the material and the collection of particles, but can differ in the approach to this process. It allows for complex and sophisticated nanoparticulate synthesis, with fast kinetics and control by varying pressures, cooling rates and the collecting mechanism. Examples of such synthesis are gas condensation, plasma and chemical vapor deposition techniques [48].

Chemical/electrochemical reductions are nanosynthesis methods that include a reduction of nanoparticulates from a solvent containing their precursors. Most notably, this is a method frequently used to generate silver nanoparticulates from their salts. Electrochemical reductions are a subtype that occur with the use of an electrochemical cell through the process of electrodeposition [49].

Inflitration methods can be separated into two main types – melt infiltrations and solvent impregnation. Solvent impregnations method base their principle upon the solubility of the material in an organic solvent. The porous material is soaked into the hydride precursors that then populate the pores and, in combination of activator, transform into the wanted material. Melt infiltration are analogous, but happen in the melt state, which requires the hydride to have a melting temperature under reasonable conditions for experimental procedures [22, 12].

For lithium alanate, the most frequent methods of nanostructuring used are high energy ball milling, composite forming, catalyst doping, and, to a lesser extent, solvent impregnation. The application of these methods and their results on improving the properties of $LiAlH_4$ will now be considered.

High energy ball milling can be varied depending on the additives used – frequently, alanate is milled in the presence of nanoparticulate catalyst (e.g. ZrC, $TiCl_3$), or a porous matrix host (metal organic frameworks, carbons). The first case is commonly reffered to as catalysed alanate, where the latter is usually an example of nanoconfinement. Some examples of such research will be given in the following subsection.

Other possibilities of nanoconfinement include *in situ* synthesis, as done by Wahab et al, on a porous carbon system with incorporated nickel particulates. This was done by the infiltration method of slow dripping of the alanate onto the porous template, homogenising, and finally drying. As with other destabilising methods, this lead to a significant decrease (the on-set dehydrogenation temperature achieved being 80 °C) in dehydrogenation temperatures, but catalytic impurities remain a concern. Rehydrogenation was not discussed [50].

Before nanostructuring, research frequently focused on producing composites of lithium alanate with another hydride (e.g. MgH_2), lithium borohydride ($LiBH_4$) or lithium amide ($LiNH_2$) to achieve better properties [12].

Research that surrounded composites with magnesium hydride indicates a formation of Al-Mg intermetallic phases that did improve the dehydrogenation properties compared to bulk $LiAlH_4$ and MgH_2, but suffering from a decrease of overall H_2 content. Compositing the alanate with magnesium hydride tampers with the reaction steps, achieving a change in the mechanism, with partial rehydrogenation becoming possible at relatively mild conditions (350 °C, 100 bar) [51]. However, the achieved dehydrogenation temperatures and lowered gravimetric H2 content of the system still make it unsuitable for practical purposes.

It is perhaps the research surrounding lithium borohydride that lead to the most interesting results. Xia et al. used nanoporous carbons to nanoconfine $LiBH_4$, reducing the onset dehydrogetaion temperatures for both relevant reversible steps, but also changing the mechanism of the reaction. The composite also showed apparent reversibility under relatively mild conditions of 100 bar and 500 °C, albeit with reduced efficiency of just 10% compared to the initial dehydrogenation step after as little as five cycles of dehydrogenation and rehydrogenation, which the authors perscribe to the liberation of diborane and aggregation of dehydrogenated products, greatly reducing their free surface and hindering kinetics [52].

Finally, it should be noted that due to its previously discussed problems in respect to its regeneration, lithium alanate is researched to a significantly lesser extent than its sodium counterpart, sodium alanate.

1.2.3. Carbon black and Vulcan XC72R

The general carbon allotropes can be defined in respect to the type of hybridisation their covalent bonds form: diamond with sp^3, graphite with sp^2, and amorphous carbon with a mixture of the two. Fullerenes, graphene, and similar forms are just modifications of the three general types [53].

Carbon materials are frequently used in nanotechnology because of their general inertness towards a variety of environments, good electrical properties, and possibility of surface chemistry, along with porosity. One such material, Vulcan XC72R (Cabot, USA), was used in the experimental work of this thesis [53].

Turbostratic structure is essentially an intermediate amorphous carbon – a mixture of graphitic sp^2 hybridised carbons enveloped by amorphous domains of both sp^2 and sp^3 hybridised carbons. Carbon black, historically the most frequent additive to rubber, is an example of such a structure. It's characterised by good tensile strength, high specific surface area, and generally lower level of impurities. Like all carbons, it's a good electrical conductor and remains mostly inert to both acids and bases [53].

Vulcan XC72R is a low-cost amorphous carbon black with a specific surface area estimated at 250 m^2/g formed as an aggregation of nanoparticles in the size range of 30 to 60 nm. Lazaro et al. determined that it had mesoporous structure, but contained a large number of micropores [54]. Considering this pore size distribution and in accordance with IUPAC nomenclature, it can be categorised as a mesoporous material (2 – 50 nm) category [54, 55]. Additionally, Vulcan XC72R has very modifiable surface chemistry and is frequently improved to achieve

better properties (e.g. thermal, electrical, chemical), which are required for efficient catalysis besides its porosity [54, 56].

1.3. Methods

1.3.1. Synthesis

The principle mechanistic synthesis mechanism used was high energy ball milling. It can be defined as "*a powder processing technique involving deformation, fracturing and cold welding of the particles during repeated collisions with a set of balls*" [57]. A schematic of the working principle during operation is presented on Figure 3.

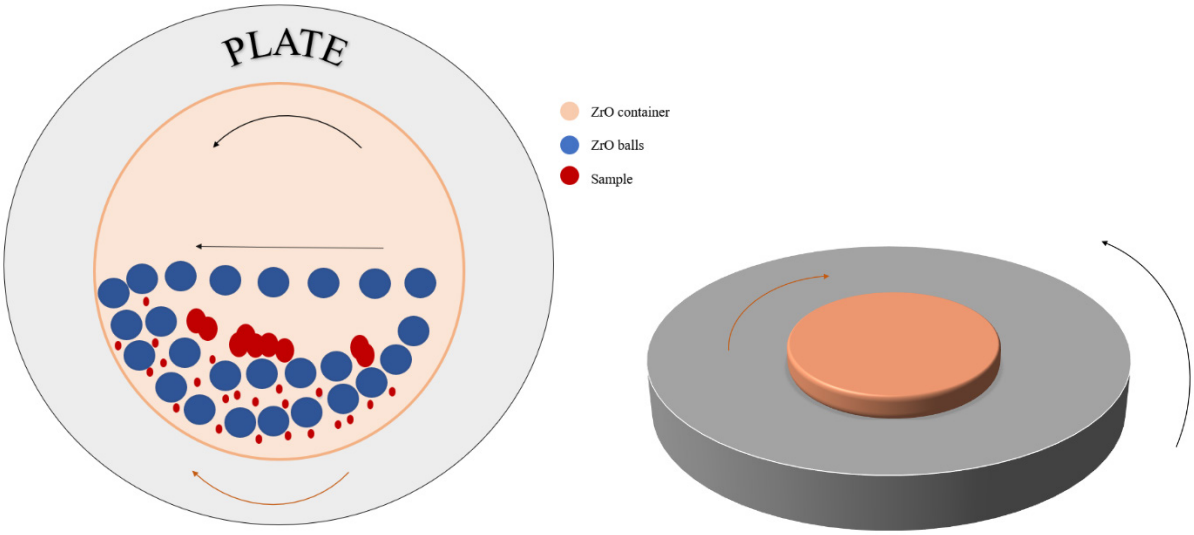

Figure 3. Ball-milling schematic. The grinding bowl and the plate rotate in opposite directions.

The gist of it is essentially quite simple and dates back to the earliest periods of human history – using mechanical forces to break things down. However, this very rarely leads to any significant chemical change – only with the appearance of fine grinding did mechanochemistry first come into light. Essentially, mechanochemical processes use a source of mechanical energy to influence chemical changes in a system, along with a structural change and particle size reduction. A mechanochemical process effectively pushes the targeted system out of equilibrium with very short relaxation times (ms and less). The accumulated energies originating from fractures, plastic deformations, elastic strain energies, relax through decomposition, alloying, or a chemical reaction. The nature of these interactions at spots of ball-material collisions depends on the nature of the grinded and grinding materials themselves (i.e. whether they are ductile or brittle, inert or reactive). The non-equilibrium characteristic of the process can lead to structures that remain stable long after the end of process [57].

A significant phenomenon of ball-milling is the observed difference between local and global temperatures. Simply put, observing a single ball-material-ball collision can lead to much higher temperatures in a moment than what is observed as an average temperature for the

system. This means that even if a supposed temperature of a system is e.g. 100 °C, locally, the temperatures can reach a several hundred degrees higher [58]. This can cause degradation and be a trigger for an (unwanted) chemical reaction [57].

In the case of lithium alanate, it should be noted that research indicates that ball-milling does not change the mechanism of the dehydrogenation reaction [59].

1.3.2. Characterisation

1.3.2.1. Temperature-programmed dehydrogenation

To obtain data on the reaction step temperatures for the amount of released hydrogen and kinetic information for the dehydrogenation of lithium alanate composites, a temperature-programmed dehydrogenation (desorption) instrument can be used. The basic principle is simple: temperature is programmed to ramp linearly over time, and an inert gas at constant flow, termed carrier gas, passes over the sample. With the increase of the temperature, hydrogen begins to release from the alanate in a step-wise fashion (see Figure 2). The released hydrogen is carried to the detector where it is recorded and quantified. In the case of the used AutoChem 2950 HP chemisorption analyser (Micromeritics, USA), the detector is a thermal conductivity detector. The detecting principle is based on different thermal conductivities of the inert carrier gas (e.g. nitrogen, argon) and the sample gas (hydrogen). On a relative scale (to air), hydrogen has a seven times higher thermal conductivity than nitrogen [60]. Due to this difference, the carrier gas removes heat from the filament of the detector more slowly, which consequently requires less electricity to maintain at constant temperature. The instrument records these changes in electrical demand over a range of temperatures, which is quantified through calibration measurements [61].

1.3.2.2. Gas sorption

The gas sorption method is one of the most common methods for determining the specific surface area (the ratio of surface to the mass of a particulate), porosity, average pore size, and pore size distributions of various materials. The nature of adsorption lies in physical interactions (i.e. physisorption) or chemical interactions (i.e. chemisorption) [62]. Physisorption relates to the Van der Waals electrostatic interactions. Chemisorption relates to chemical changes and forming/dissociation of chemical bonds.

The main gas adsorption theory on solid surfaces used for the calculation of the specific surface area is the BET theory, named after the principal researchers behind it – Brunauer, Emmett, and Teller. It's effectively a continuation of the Langmuir monolayer adsorption theory, positing multilayers instead of singular one. The main hypotheses of this theory are:

1. Gas molecules physically adsorb on a solid in an infinite number of layers
2. Gas molecules interact only with adjacent layers
3. The Langmuir theory is applicable to every layer

4. The initial enthalpy of adsorption (first layer) is constant and greater than the succeeding ones

5. The enthalpy of each following adsorption is the same as the enthalpy of liquefaction (vapour → liquid).

Most commonly, the gas used for gas adsorption measurements is nitrogen. The measurements can be static or dynamic, and the measured specific surface areas can range from 1×10^{-3} to 10^3 m^2/g [63].

By analysing the adsorption isotherm – plot of equilibrium adsorption capacity with pressure under constant temperature – specific surface area can be calculated through the BET theory, using the following linearised BET equation:

$$\frac{p}{X(p_0 - p)} = \frac{1}{X_m C} + \frac{(C-1)p}{X_m C p_0} \quad (1)$$

where p is the equilibrium gas pressure of the measurement (belonging to a range of equilibrium pressures that form the isotherm), p_0 is the saturation vapor pressure of gas at the adsorption temperature, p/p_0 is the relative pressure, X is the adsorption capacity (in gravimetric or volumetric units) at partial gas pressure of p, X_m is the saturated adsorption capacity for the monolayer adsorption, and C is the BET constant.

By plotting a $\frac{p}{X(p_0-p)} - \frac{p}{p_0}$ plot, X_m can be determined as $X_m = 1/(a+b)$, where the coefficients a and b are calculated from the intercept and the slope respectively. Under some conditions, the constant C is large enough that the intercept can be ignored.

The total surface area can be calculated as:

$$S = \frac{X_m N A}{M} \quad (2)$$

Where N is the Avogadro constant (6.023×10^{23} molecules/mol), A is the section area of the adsorption molecule, and M is the molecular mass of the adsorption molecule.

The specific surface area and the volume specific surface area can be calculated as:

$$S_M = \frac{S}{M_X} \;\; OR \;\; S_V = \frac{S}{V_X} \quad (3)$$

Where S is the total surface area, and S_M and S_V specific surface are in respect to mass and volume respectively. M_X and V_X are the sample mass and volumes respectively.

BET theory also allows for the determination of the equivalent pore size through the pore shape coefficient and porosity.

An illustration is presented on Figure 4.

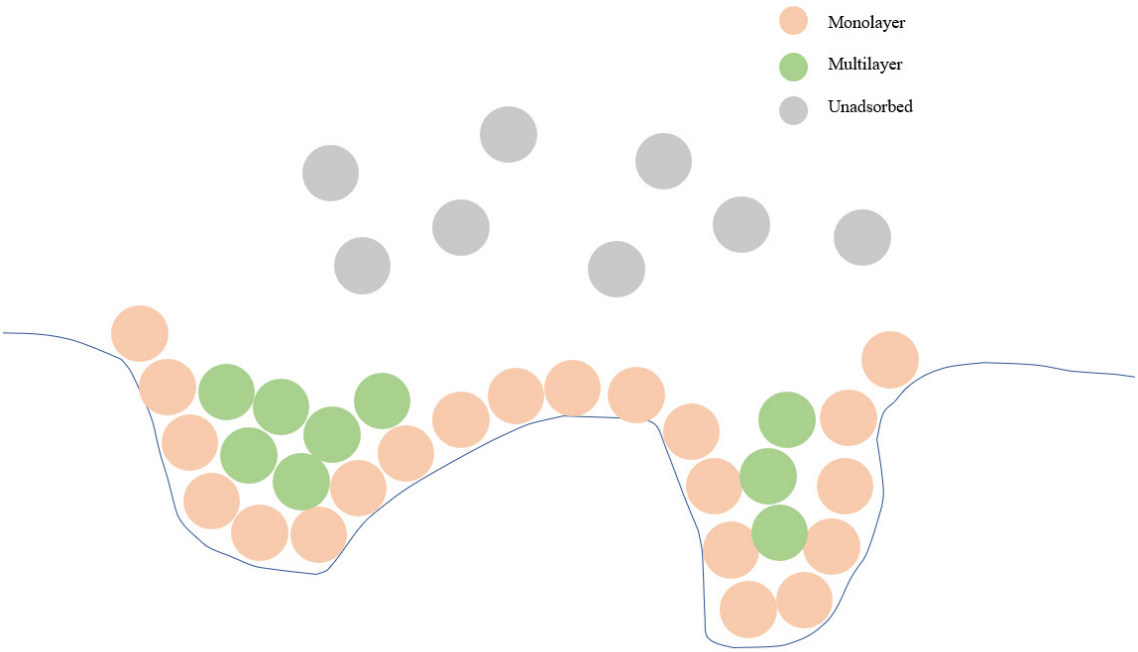

Figure 4. BET adsorption illustration.

1.3.2.3. X-ray diffraction

X-ray diffraction (XRD), being one of the revolutionary techniques of the 20th century, is still one of the most widely used methods of determining the crystal structure of a material, along with the mean positions of atoms in the crystal and various other information. X-ray diffraction is based on constructive interference of monochromatic X-rays from a crystalline sample. The X-rays are generated through a complex system of a cathode ray tube, monochromators, and lenses. By heating the filament, electrons are created and accelerated towards the anode, which in turn produces X-rays. The X-rays then bombard the sample. The X-rays interact with the crystal's atom's electrons which constructively scatter i.e. diffract (due to the order of the crystal structure). From the outgoing angles and intensities of the diffracted beams, a diffractogram can be constructed which is a function of the density of electrons within the crystal. From this image, the previously mentioned positions of atoms can be deduced, along with other crystallographic information [64].

The basis of XRD is the interaction of the incoming X-rays with the sample through constructive interference when Bragg's law is satisfied:

$$n\lambda = 2dsin\theta \quad (2)$$

where n is the diffraction order (a positive integer), λ is the incoming X-ray wavelength, θ is the angle between the sample plane and the X-ray beam, and d is the distance between lattices. The following schematic presents a visual representation of the diffraction and the Bragg's law (Figure 5).

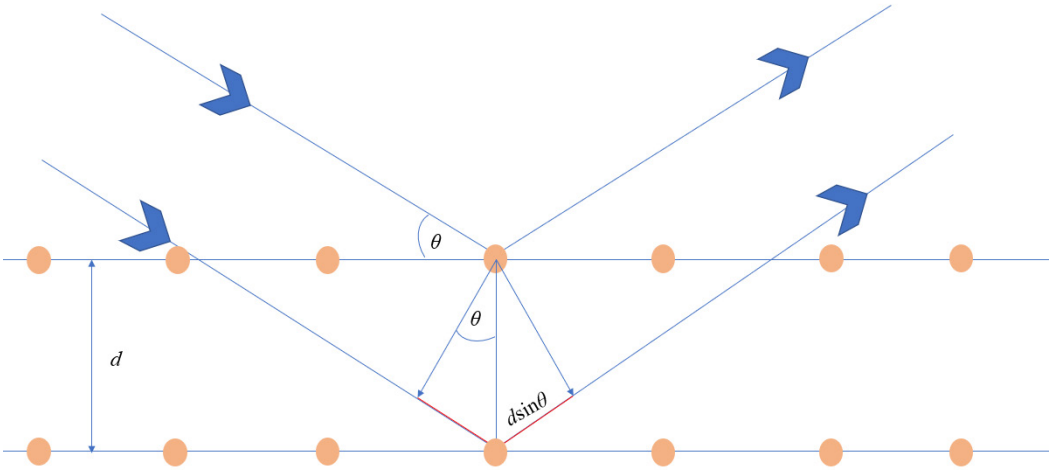

Figure 5. Bragg's law schematic, where two beams with same wavelength hit the crystalline solid under angle θ and scatter off two atoms (here central); the lower beams travels an additional distance of $d\sin\theta$, where d is the distance between two crystal planes.

Powder X-ray diffraction is a variant of the XRD process where the diffraction pattern is obtained from a powder of the material, rather than an individual crystal. This allows a wider field of application since it dismisses the need to make individual crystals. The attained diffraction pattern is obtained from a material in which the crystals are randomly aligned, hence serves as an averaged over all crystal aligments pattern, as opposed to a single crystal one [65]. Due to the radiation scattering around these randomly oriented crystals, the pattern is obtained in the form of Debye-Sherrer rings (an intersection of the recorded diffraction cones that all have the same apices, with a plane orthogonal to the cones' axis), as opposed to discrete spots in single crystal diffraction [66].

2. Experimental section

2.1. Synthesis of composites

Lithium alanate ($LiAlH_4$, Sigma Aldrich, pellets, reagent grade, 95%) was combined with Vulcan XC72R (Cabot, USA) via ball milling in a Pulverisette 6 classic line planetary mono mill (Fritsch, Germany) for 40 minutes, with 10-minute cooling breaks after every 5 minutes. The usual conditions of ball milling were 400 rpm over 8 cycles, 5 min of milling each. Sample preparation and retrieval was performed in argon atmosphere (Ar, 5.0, Linde, UK) in a MBraun LABmaster sp glovebox (MBraun, Germany). The ball milling grinding bowl was hermetically sealed with mechanical clamps to keep the air out. 25 ZrO_2 grinding balls with diameter of 10 mm were used with a ZrO_2 grinding bowl for the ball milling process. Composites were synthesised in this way containing 20, 30, 40, 50, 60, 70, 80 wt% lithium alanate, the remaining weight content being Vulcan XC72R.

Ball milling parameters were varied in case of the composite with 40 wt% of lithium alanate to investigate the wider impact of ball milling parameters on the dehydrogenation kinetics of the composites. More specifically, the difference between the 300 rpm and 400 rpm was determined, along with the number of cycles – four in comparison to the normally used eight.

2.2. Temperature-programmed dehydrogenation

Dehydrogenation experiments were done with the AutoChem 2950 HP chemisorption analyser (Micromeritics, USA) using a thermal conductivity detector. Small amounts (approx. 15 mg) of synthesised composites were placed in a stainless steel sample holder under argon atmosphere. The sample holder was then temporarily sealed and transferred to the instrument. Sample holder was under constant nitrogen gas flow at a rate of 50 ml/min (N_2, 6.0, Linde, UK) and cooled to 0 ℃ using liquid nitrogen, where it was held for 2 h to establish a baseline. A temperature ramp of 2 ℃/min was imposed, and the H_2 concentration in the gas flow was measured from 0 to 600 ℃. Data was treated and plotted using OriginLab 2020b (OriginLab Corporation), where the efficiencies were calculated from the integrated area of the w_{H_2}/T vs. T plot, where the calculated efficiencies are in reference to the theoretical maximum amount of H_2 in the composite, w_{max} = 0.106 g_H/g_{LiAlH_4} (the mass ratio of hydrogen in $LiAlH_4$).

2.3. Powder X-Ray diffraction

Composites and their constituent materials were analysed using powder XRD. The measurements were performed with a D8 Advance (Bruker, USA) diffractometer using a low-background airtight specimen holder. Ni-filtered Cu Kα radiation was used and detected with a LynxEye detector. Measurements were done in the range of 13-80° 2θ with a step of 0.016°. Measurements and preliminary data analysis were performed by Mr. Jaan Aruväli from the Department of Geology at the University of Tartu, using the software package Diffrac Suite EVA and the PDF4+ 2020 database.

2.4. Cycling (rehydrogenation)

To attempt to rehydrogenate the composite sample, an iSorb HP1 (Quantachrome, USA) high-pressure gas sorption system was used. This is a volumetric high-pressure gas sorption instrument equipped with pressure sensors of high sensitivity that allow for monitoring of changes in pressure compared to the well-defined manifold volume and stable temperature control. The system's own software calculates the differential pressure between the theoretical and actual pressures in an increment of time, the difference being in this case the amount of hydrogen stored or released [67].

About 200 mg of the composite was placed into the instrument's sample holder inside the glovebox (inert Ar atmosphere) and attached to the machine. It was then subjected to 180 bar of H_2 under 150 ℃, with a ramp rate of 10 ℃/min.

2.5. Gas sorption

Composite samples were analysed using the N_2 sorption method with the 3FLEX (Micromeritics, USA) adsorption analyser instrument. The sample holder was filled with approximately 150 mg of sample under argon atmosphere. The sample holder was hermetically sealed and transferred to the instrument where it was *in situ* degassed for 24 h under vacuum and at 40 ℃ achieved by use of a heating mantle. A programmed measurement was initiated, and liquid nitrogen (77 K) was used to perform the measurement. Specific surface area (S_{BET}) was calculated through the BET theory application of the instrument's software package, while the porosity parameters (V_{tot}) were calculated from the adsorbed amount corresponding to p/p_0 = 0.95. This allows for estimation of pores that are less than 40 nm in width.

3. Results and discussion

3.1. Temperature-programmed dehydrogenation

Temperature-programmed dehydrogenation results will be considered in respect to composition effects of fresh samples (the measurement being done immediately post-synthesis) and time effects for particular compositions of composite. Composition effects are of value due to the expected connection between the improved H_2 storage and release properties and the presence of carbon scaffolding. Time effects meanwhile could indicate a level of metastability of lithium alanate in storage.

All efficiencies discussed in this section are calculated as the efficiency of the H_2 released in comparison to the theoretical maximum.

3.1.1. Composition effects

The temperature-programmed dehydrogenation for different composite compositions (and pristine lithium alanate) are shown on Figure 6, 7, and 8. Furthermore, on-set dehydrogenation temperatures and efficiencies of composites are presented in Table 3.

Interpretation of Figure 6 and the comparison between mortared, ball-milled $LiAlH_4$ and the highest wt% composite (80 wt%) is reasonably straightforward – ball-milling reduces particle size; the increased surface area of the particulates compared to mortared $LiAlH_4$ helps the kinetics of dehydrogenation (Table 6, Ch. 3.2.), which is reflected in the lower dehydrogenation on-set temperatures. The peaks (their maximum points) of this relase (belonging to R1) can be compared as 164 °C (mortared) vs 147 °C (ball-milled). Efficiencies remain relatively close to each other and high throughout (92% vs 91%), where the slight decrease in efficiency is expected due to mechanical stresses that occur and degrade the alanate during ball milling. The 80 wt% composite meanwhile shows a significantly larger decrease of dehydrogenation on-set temperature (to 120 °C), indicating that even with a 20 wt% presence of carbon black, there exists a significant amount of confinement within the carbon's pores, along with interactions with the scaffold. Dehydrogenation on-set temperature decrease is expected, but what is interesting is that the apparent efficiency (95%) of the 80 wt% composite is not significantly lower than its bulk counterparts, which is likely due to a degree of stabilisation within the carbon scaffold during milling. The peak belonging to R3 step makes the perhaps the most significant shift compared to pure $LiAlH_4$ samples – from 485 °C for the mortared bulk $LiAlH_4$, through 455 °C for the ball-milled $LiAlH_4$, to finally 340 °C for the 80 wt% sample, indicating that the change with even a small amount of carbon black present is significant on the dehydrogenation properties of the material. It should also be noted that the curves are sharp and well-defined, which is something that will be of importance in the following passages of the analysis of lower weight percentage (of $LiAlH_4$) composites.

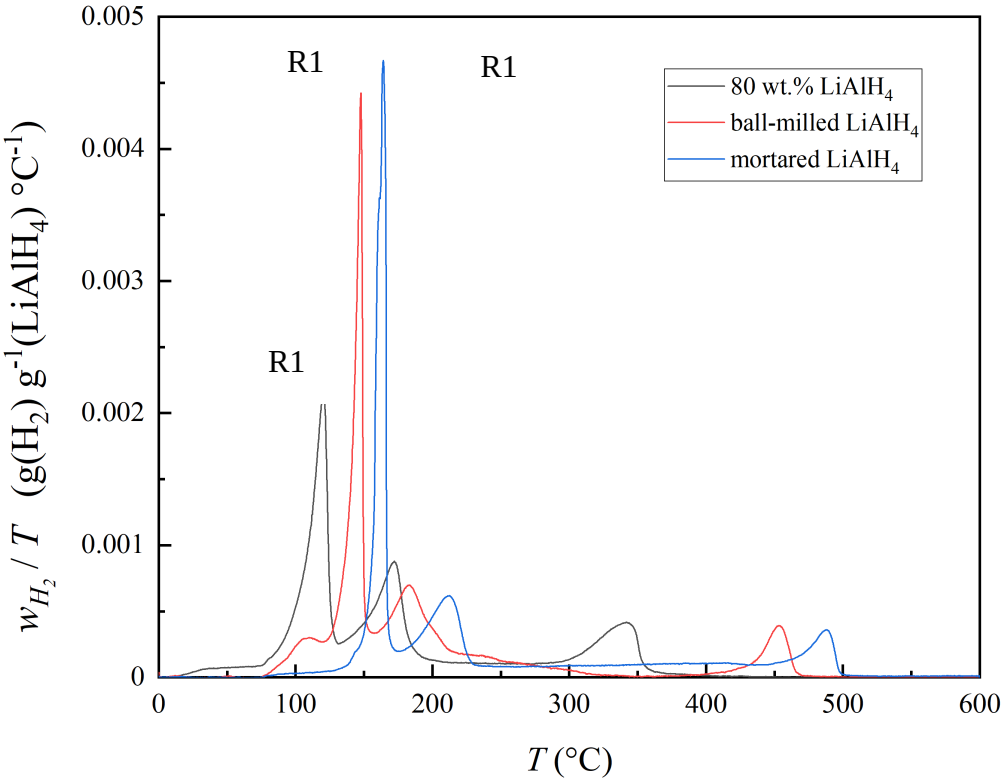

Figure 6. Mass of released hydrogen normalised to the overall mass of $LiAlH_4$. Pristine, mortared $LiAlH_4$ compared with ball-milled $LiAlH_4$[7], and 80 wt% $LiAlH_4$ composite

Figure 7 portrays a so-called transition range, in the sense that the curves retain the shape of bulk material, however certain „quirks“ of confiment show their face. Most notably, this is evident on the 60 wt% sample – the first peak is broader and doesn't dominate the process, which would suggest a significant degradation during the ball milling or a high enough lowering of the dehydrogenation temperatures that it occurs „prematurely“ (i.e. before the measurement). However, that is not the case – the efficiency remains steadily at 92%, and upon the closer observation of the curve, it is apparent that the H_2 release is no longer strictly confined to the traditionally well-defined two peaks (corresponding to R1 and R2, as described in Figure 2) – implying an existence of more amorphous regions of confined $LiAlH_4$ that release H_2 continously in a wide temperature range, connecting (coalescing) the two usually separated R1 and R2 peaks. Curiously, the R3 peak remains relatively constant during the change from 80 wt% to 60 wt% of alanate content.

[7] All ball-milled samples (ball-milled $LiAlH_4$ and all the composites) were ball milled using the following parameters: 400 rpm, 8 cycles, with 10 minute pauses between cycles.

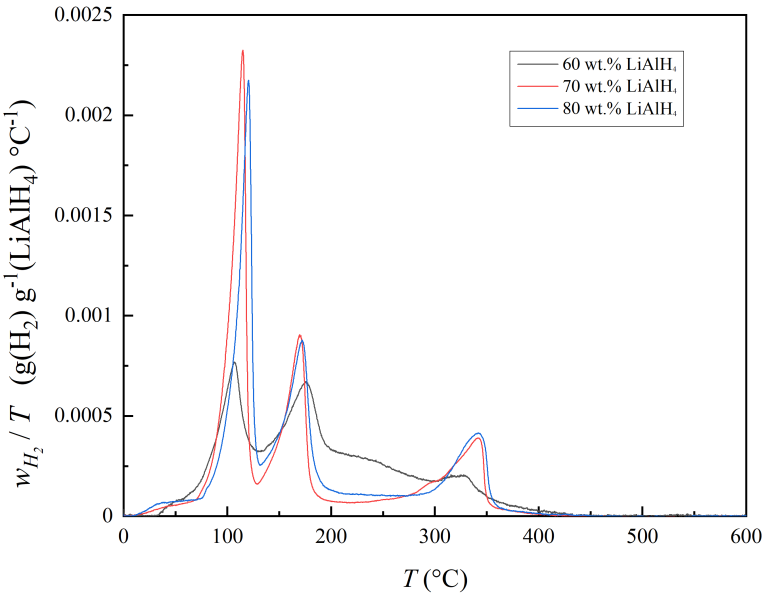

Figure 7. Mass of released hydrogen normalised to the overall mass of $LiAlH_4$. Comparison of composites with 60 wt%, 70 wt%, 80 wt% $LiAlH_4$.

This only becomes more evident on Figure 8 – all the composites below 60 wt% of $LiAlH_4$ show the aforementioned continuous release of H_2, not bound by any explicit peak. They do however, have some other peculiarities which will now be discussed. Mostly, this comes in the peculiar loss of the peak characteristic for the high temperature step 3 (R3, as described in Figure 2), the lower the mass ratio of $LiAlH_4$ in the composite is. The 50 wt% composite is the first one to exhibit an increasingly „noisy“ signal, which is likely due to the fact that lower $LiAlH_4$ wt% composites release less H_2 – resulting in a decrease of total signal. With lower total signal, the „noise“ increases. The 50 wt% composite also shows H_2 release from near-ambient temperatures upon heating, even before the main R1 peak (as observed in its hump-like shape) – something that reoccurs on the 20 wt% sample, likely suggesting an amorphous component. The overall broadening of the peaks can be attributed due to areas of sample – e.g. more crystalline versus amorphous areas of trapped $LiAlH_4$ – showing different thermodynamic properties, leading to uneven temperatures, hence different hydrogen evolution kinetics.

The 40, 30, and 20 wt% samples meanwhile do not exhibit a well-defined third peak (R3 step). This isn’t particularly likely, considering that the R3 step is highly endothermic and the reaction is not expected to occur before the previous two reaction steps no matter how destabilised the sample might be. Considering that the efficiency (Table 4) of these composites isn’t so low as to indicate a complete loss of the hydrogen „stored“ in the third reaction (as described in Figure 2 as R3), and which contains about approximately 2.7 wt% of total hydride mass, roughly a quarter of total stored hydrogen, it can be supposed that the hydrogen corresponding to it is being released without a clear peak in the sub 300 °C range.

Additionally, the release of H_2 for these samples begins at much lower temperatures, frequently at room temperature (and in the case of 20 and 50 wt% even lower temperatures, as evidenced by the aforementioned shoulder on R1), further proving the destabilisation of the confined $LiAlH_4$.

It is obvious that the lower the mass ratio of $LiAlH_4$ in the composite, the more confined $LiAlH_4$ is expected to be within the pores of Vulcan XC72R. This will be later on supported in the section related to the gas sorption measurements. The interactions with the carbon scaffolding should similarly increase in the case of higher carbon loading. However, this leads to a larger destabilisation of the alanate and freer, spontaneous decomposition. The efficiency falls as low as 57% in the case of the 20 wt% composite (Table 4).

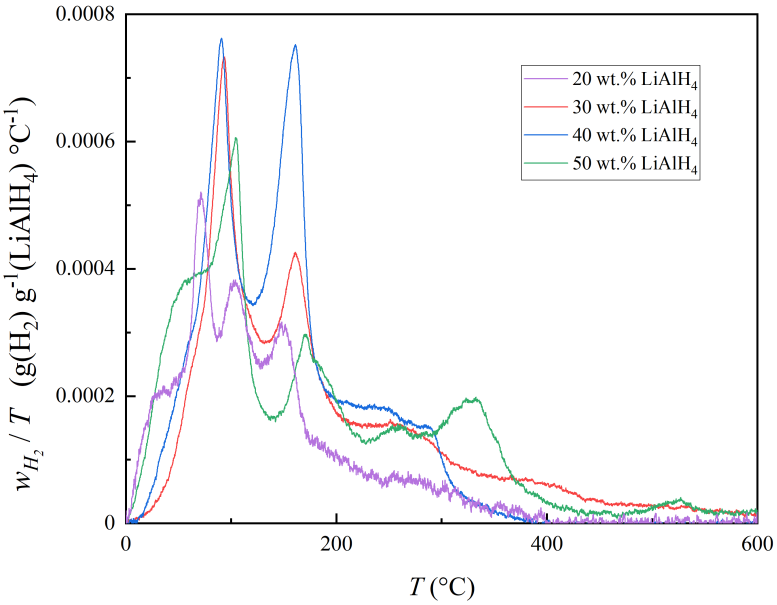

Figure 8. Mass of released hydrogen normalised to the overall mass of $LiAlH_4$. Comparison of composites including 20 wt%, 30 wt%, 40 wt%, and 50 wt% $LiAlH_4$.

Table 3. Temperatures of peak maxima (belonging to R1) for composites from 20 – 80 wt% of $LiAlH_4$, in increments of 10 wt%, and mortared and ball-milled bulk LiAlH4. Efficiencies of the same composites, as calculated to the theoretical maximum (w_H = 0.106 g_H/g_{LiAlH_4}).

wt% of $LiAlH_4$	**T_{R1}, °C**	**efficiency, %**
100 (mortared/ball-milled)	164, 147	92, 91
80	120	95
70	115	91
60	107	92
50	103	83
40	91	83
30	92	78
20	71	57

3.1.2. Ball milling effects

Temperature-programmed dehydrogenation investigations were also done to determine the effect of the ball milling procedure on the *T* of H_2 release. These were performed on a composite consisting of 40 wt% $LiAlH_4$. A variation on the usual ball milling parameters of 400 rpm and 8 cycles was done – 300 rpm and 8 cycles, along with 300 rpm and 4 cycles were used.

Figure 9 shows quite predictable results – 8 cycles as opposed to 4 cause lower on-set dehydrogenation temperature, due to a larger level of confinement and nanostructuring achieved, while 400 rpm further increases the confinement in comparison with the 300 rpm conditions, by physically increasing the chance of confinement due to increased mechanical contact between the alanate and the carbon. Interestingly, one would expect that the harsher, longer conditions would lead to a diminishment in efficiency in the 400 rpm and 8 cycles sample. But this is not the case – the calculated efficiencies (83% / 77% / 74%) of all three samples (400 rpm, 8 cycles / 300 rpm, 4 cycles / 300 rpm, 8 cycles) do not show significant variation[8] from one another and, thus, the more harsher ball milling conditions do not cause considerable decomposition of $LiAlH_4$.

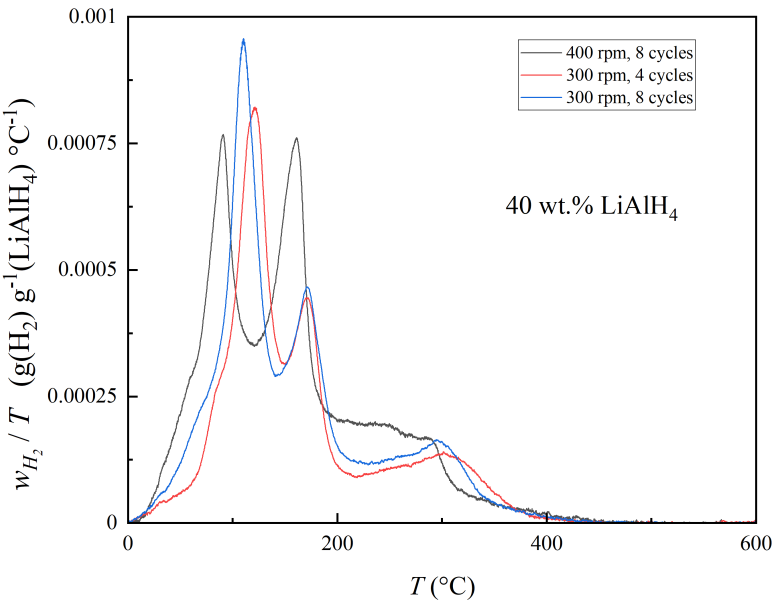

Figure 9. Mass of released hydrogen normalised to the overall mass of $LiAlH_4$. Different ball milling conditions.

[8] The existing difference can be explained by the possibility that some of the samples might have spent a longer time in storage before measurement. The effect of storage will be explored in detail in the following subsection.

3.1.3. Time effects

Figure 10, 11, and 12 deal with the effect of time spent in storage for three different composites – 40, 30, and 20 wt% respectively.

Figure 10 shows a diminished peak corresponding to R1, which is to be expected considering the expected low exothermic enthalpy of this first step reaction (considering that the heating rate of the material was 2 °C/min; see: Ch. 1.1.2). This is something that translates to the measured efficiency of this composite, as presented in Figure 13. An interesting observation comes to the seeming movement of the second peak, which will be further elaborated in the section dealing with the XRD results.

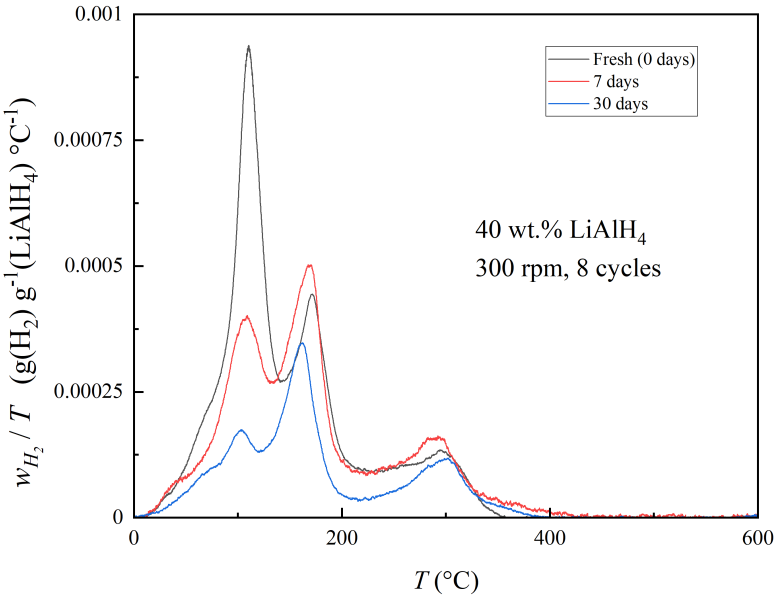

Figure 10. Mass of released hydrogen normalised to the overall mass of $LiAlH_4$. Recorded on the 40 wt% $LiAlH_4$ sample after synthesis (300 rpm, 8 cycles), 7 days, and 30 days in storage.

Figure 11 shows the H_2 release behaviour of the 30 wt% sample at various storage times after the ball milling. This particular sample is of significance because temperature-programmed dehydrogenation measurements were done more frequently to determine when the equilibrium (or rather, the *apparent* equilibrium, in line with the metastable phenomena described in Ch. 1) is reached. From Figure 12, and with further evidence from Figure 13 it can be seen that only after 14 days, the efficiency of H_2 release remains constant within the margin of uncertainty. This is somewhat unexpected – previously predicted time necessary for such an equilibrium was judged at more than 30 days (hence why other samples measured in time were in measured only after a month in storage was passed), yielding strong evidence that these composites are even more destabilised than previously considered.

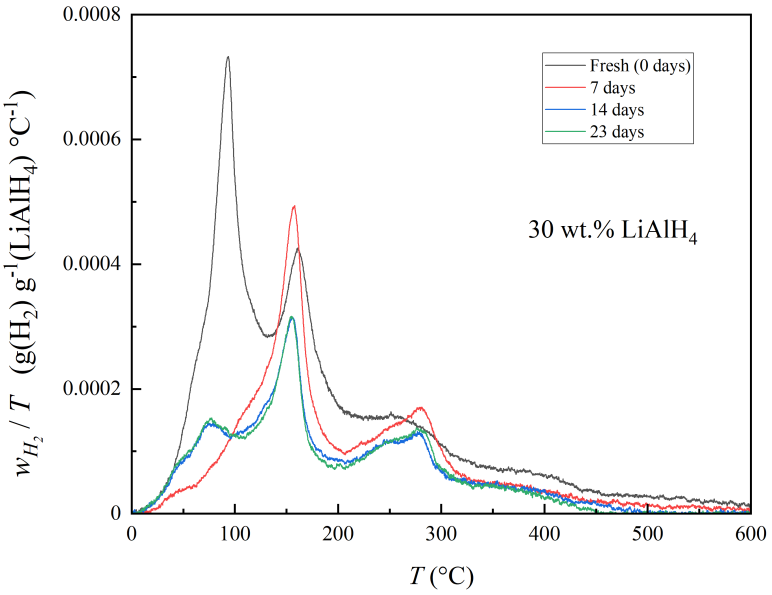

Figure 11. Mass of released hydrogen normalised to the overall mass of $LiAlH_4$. Measured from the 30 wt% $LiAlH_4$ sample after synthesis (400 rpm, 8 cycles), 7 days, 14 days, and 23 days in storage.

Figure 12 shows the behaviour of the 20 wt% sample in time. The sample shows radically decreasing amounts of H_2 with increased storage time, indicating that it is highly destabilised. The data recorded is too limited to lead to any more specific conclusion – only thing that could otherwise be noted is that the peaks corresponding to R2 are split into two, and that with the passing of time spent in storage the peak maxima decrease towards slightly lower T values. The H_2 release peak corresponding to R1 decreases in intensity (i.e. the amount of released H_2). Efficiencies are presented in Figure 13 visually and through a table included within. General trend is that the higher the $LiAlH_4$ content, the more efficiency the systems retain. This is especially evident in comparison of the 20 wt% and 30 wt% systems – suggesting that the carbon scaffolding indeed plays a large part in the destabilisation of these systems.

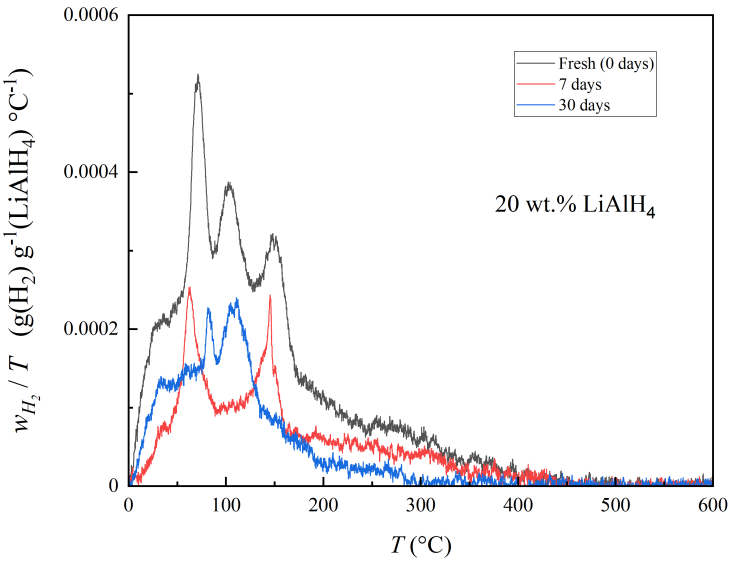

Figure 12. Mass of released hydrogen normalised to the overall mass of LiAlH4. Recorded on the 20 wt% LiAlH4 sample after synthesis (400 rpm, 8 cycles), 7 days, and 30 days in storage.

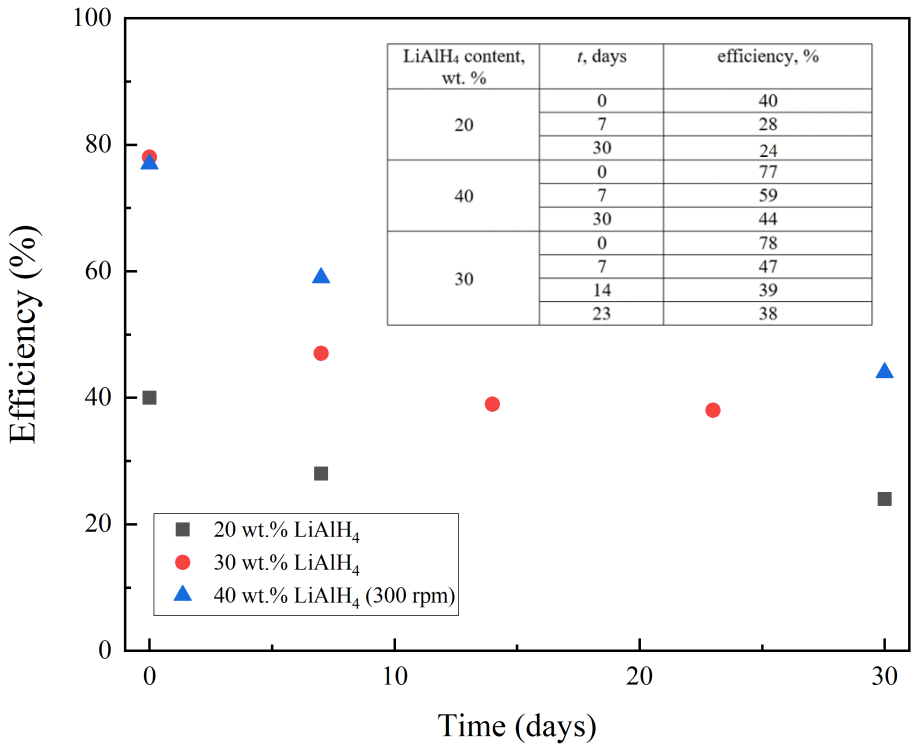

$LiAlH_4$ content, wt. %	*t*, days	efficiency, %
20	0	40
	7	28
	30	24
40	0	77
	7	59
	30	44
30	0	78
	7	47
	14	39
	23	38

Figure 13. Efficiency comparison of the 20, 30, 40 wt% composites at different points in time. Efficiencies are calculated to the theoretical maximum (w_H = 0.106 g_{H2}/g_{LiAlH4}). Ball milling conditions for the 20 and 30 wt% composite being 400 rpm over 8 cycles, and for the 40 wt% composite 300 rpm over 8 cycles.

3.1.4. Rehydrogenation effects

Figure 14 shows that the rehydrogenation procedure described in the Experimental section was not successful in regenerating the sample, but rather was countereffective in the sense that it only degraded it. There is a noticeable loss of H_2 across the whole measurement, where the largest losses appear at 150 °C, approximately belonging to the R2 step. This will be further considered in the X-ray Diffraction section.

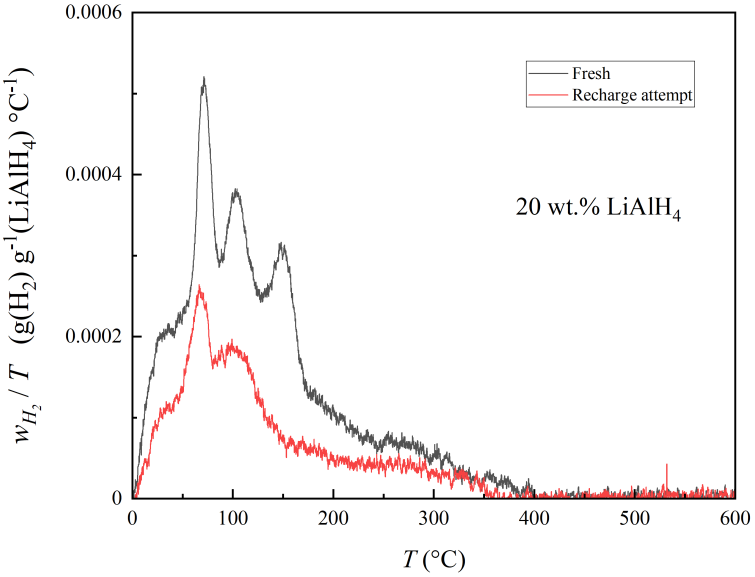

Figure 14. Mass of released hydrogen normalised to the overall mass of $LiAlH_4$ in time. Recorded on the 20 wt% $LiAlH_4$ sample after synthesis (400 rpm, 8 cycles). Recharged line corresponds to the freshly synthesised composite sample upon which a recharge procedure was attempted.

3.2. Gas sorption

Results of the gas sorption analysis showed a distinct reduction in the value of the specific surface area (S_{BET}) and total pore volume (V_{tot}) after the composite synthesis, suggesting that the pores were indeed occupied with the deposited $LiAlH_4$.Considering the wide composition ranges (20-80 wt% $LiAlH_4$), this happens to a varying extent, as expected. However, it should be noted that considering that the results presented in Table 4 were recorded after more than 30 days from the composite synthesis – further decomposition and, thus, phase separation, should be present. But considering the results previously presented, this time period spent in storage should be sufficient for the sample to have reached a certain stable equilibrium, hence the time factor should be excluded.

If we consider for example the 80 wt% sample, one would expect the specific surface area value to be much closer to the pure alanate, suggesting a complete filling of available carbon pores – however, this is not the case. Additionally, a qualitative comparison with theoretical

S_{BET} values are presented – the $S_{BET,\ theoretical}$ value being calculated through the application of the simple Voigt model of the Law of Mixtures[9] [68]. This confirms that the reduction in specific surface area is more significant than it would be if it was due to the simple addition of mass, indicating that the alanate indeed occupies the pores of the carbon.

Theoretical maximum for the single layer filling of Vulcan XC72R with lithium alanate is 31.2 wt% (i.e. g($LiAlH_4$)/g(carbon); based on alanate's density of 0.917 g/cm^3 and the total pore volume, V_{tot}, of Vulcan). It is then expected that lower wt% composites show significantly different properties than the higher wt% ones where behaviour closer to bulk alanate is expected.

Table 4. All gas sorption data recorded after more than 30 days of composite synthesis. These can be considered stable values, after the spontaneous decomposition to an equilibrium state.

$LiAlH_4$, wt%	**S_{BET} (m^2/g)**	**$S_{BET,\ theoretical}$ (m^2/g)**	**V_{tot} (cm^3/g)**
100	8	8	0.02
80	31	52	0.07
70	46	73	0.10
60	60	95	0.13
50	59	117	0.15
40	84	139	0.17
30	90	161	0.15
20	109	182	0.20
0	226 [10]	226	0.34

Furthermore, results presented in Table 5 showcase the change in S_{BET} over a storage period of days – the results were recorded in the moment of synthesis, after a week, and after a month of the synthesised sample being in storage. Over time, lithium alanate decomposes and hydrogen evolves from it; the decomposition products migrate together, freeing up the carbon surface for the adsorption of N_2. This results in higher S_{BET}. An additional explanation for this trend could be that, while in storage, the total mass of the sample decreases slightly due to decomposition and evolution of H_2, changing the overall density of the material – however, due to overall low hydrogen presence, this should not be too impactful. It is then safe to conclude that the effect of time spent in storage of these samples is not insignificant, suggesting that the sample themselves are indeed destabilised upon synthesis.

[9] Due to the simplicity of the Voigt model and the fact that other surface phenomena are involved, this is used only to show a qualitative difference of the observed results to the supposed values if things really were that simply modelled. It should not be viewed as any sort of definite quantitative analysis.
[10] Data adopted with Mr. Kenneth Tuul's permission from [69].

Table 5. All gas sorption data recorded on a 20 wt% $LiAlH_4$ composites, at different points in time.

Age (days)	S_{BET} (m^2/g)	V_{tot} (cm^3/g)
0	52.07	0.121
7	88.69	0.156
30	108.91	0.200

Additionally, gas adsorption isotherms for all samples are available in Supplementary Information, section 1.

3.3. Powder X-ray diffraction

X-ray diffraction results are presented in the following sub-sections, corresponding to discussed topics under 4.2. It should be noted that some of the values presented in the following subsections serve more as an indicator of underlying phenomena and are a part of qualitative analysis, rather than being a hard quantification. This is partly due to the fact that hydrogen and lithium are notoriously „invisible“ to X-rays due to low X-ray scattering length caused by low electron density, so overestimation of other components of these composites is expected. Additionally, amorphous zones which were previously discussed are similarly undetectable.

An example of refinement is available in Supplementary information, section 2.

3.3.1. Composition comparison

An example plot of XRD results for chosen composites is presented in Figure 15. $LiAlH_4$ peaks remain too low for easy detection (the calculated wt% content being below 1% for all samples), which, considering that the XRD measurements were performed after more than 30 days of the samples being held in storage, is not surprising. The intensities recorded, with knowledge of behaviour described in TPD section, then, can be viewed as a picture of the equilibrium state. Considering that only Li_3AlH_6 is observed, this confirms the previously discussed decrease in the R1 peak values (see Ch. 3.1.3) during long storage.

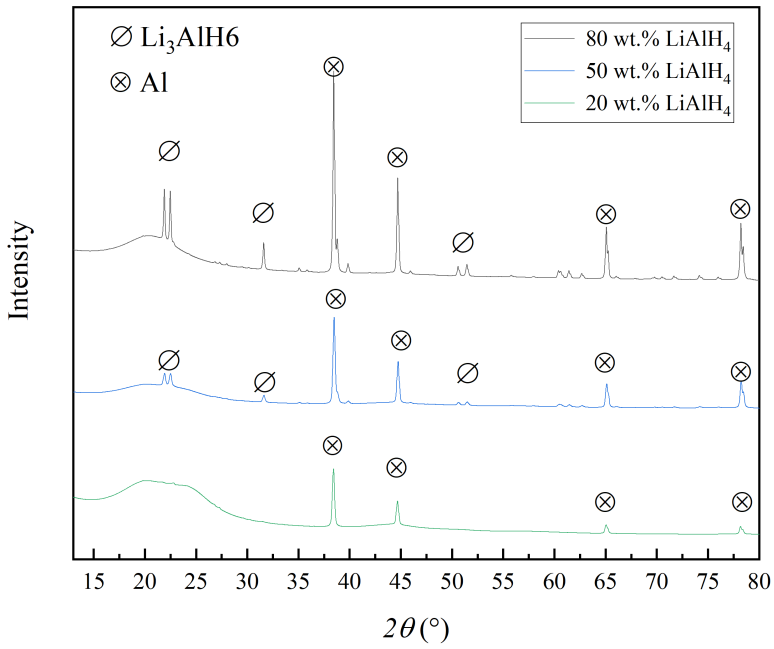

Figure 15. XRD pattern of the 20, 50, 80 wt% samples with marked characteristic peaks of Li_3AlH_6 and Al. All samples were analysed after more than a month in storage.

3.3.2. Ball milling

Results of XRD measurements for the ball milling variation series are presented in Table 6 – observing intensities of the signal does not give any relevant data, likely due to the overall similarities of the samples. However, the crystallite size (calculated through a Double-Voigt fit approach, using FWHM and the Lorentzian function[11]) indicates the overall trend of smaller particulates under higher intensities / longer duration ball milling conditions. This corresponds well with the TPD data previously discussed – the smaller the crystallites, the easier the desorption can occur, resulting in lower dehydrogenation temperatures, be it the dehydrogenation on-set temperature or temperatures corresponding to step R2. It is worth noting though that the 15 nm value corresponding to $LiAlH_4$ is most likely a vast underestimation (see: uncertanties in Footnote 12) – probably a combination of factors such as overall degradation during milling, the XRD „invisibility“ of Li and H, and segregation into amorphous, undetectable zones.

[11] In-built within the TOPAS software, for more see [70]

Table 6. Crystallite sizes for different composite samples (40 wt% $LiAlH_4$) where ball milling parameters were varied.

Ball milling parameters	Al, nm	Li_3AlH_6, nm	$LiAlH_4$[12], nm
400 rpm, 8 cycles	108	25	15
300 rpm, 8 cycles	140	65	112.9
300 rpm, 4 cycles	130	78	107.5
400 rpm, 4 cycles	167	52	15

3.3.3. Time

XRD results presented on Figure 16 on the time variation series indicate that the aluminium content increases and $LiAlH_4$ decreases during storage, which confirms degradation of the material, i.e. the R1 reaction taking place in storage. The Li_3AlH_6 can only be visibly detected on the spectrum for the 40 days sample, hence it is the only placed where it was marked. Table 7 specifies the calculated composition changes. The change in Vulcan content should not be taken as anything other than a relative change due to the increased „invisibility“ of phases with the decomposition of the sample.

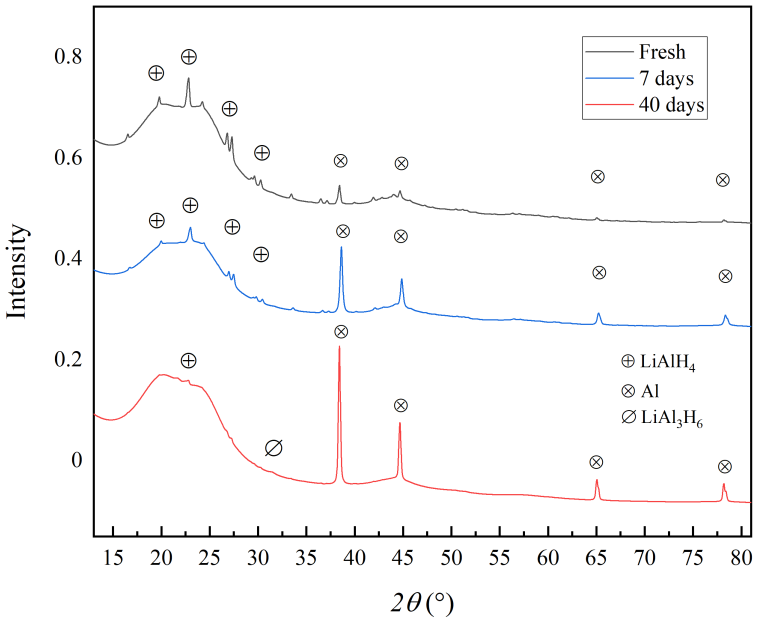

Figure 16. XRD results gathered for the 20 wt% sample, at differents in time (fresh vs. spending time in storage). Marked are the characteristic peaks for $LiAlH_4$ and Al. Hexahydride peaks are uninteligible.

[12] To further illustrate this point, the fitting uncertainties for $LiAlH_4$ are presented as 10.7/139.4/41.3/2.7 (nm) respectively.

Table 7. Composition of 20 wt% composites at different points in time, as calculated by Rietveld refinement.

days	Al, %	Vulcan, %	Li_3AlH_6, %	$LiAlH_4$, %
0	1.33	89.9	1.4	7.37
7	7.89	85.2	1	5.9
40	11.2	85.5	2.6	0.67

3.3.4. Rehydrogenation

As described in the experimental section, certain composite samples underwent a procedure of rehydrogenating at 180 bar of H_2 under 150 °C, with a ramp rate of 10 °C/min for 48h. TPD results showed that the only thing that occured was further degradation of the material – this seems to be confirmed on Figure 17. Considering that the $LiAlH_4$ signal on the XRD diffractogram is invisible, yet still appears as the R1 peak on Figure 14, it can be assumed that the alanate is trapped as amorphous or small crystallite. Meanwhile, the recharged sample shows a barely noticeable hexahydride signal, yet the R2 peak is not expressed as a clear peak in Figure 14 – this could mean that the hexahydride (Li_3AlH_6) has a tendency of segregating into crystal zones rather than being amorphously contained.

Furthermore, a renewed attempt was made to recharge the material after it reached the 40 days – Figure 18 doesn't show any indicator of success. It is safe to say that a revision in the rehydrogenation conditions requires further investigation, if at all possible.

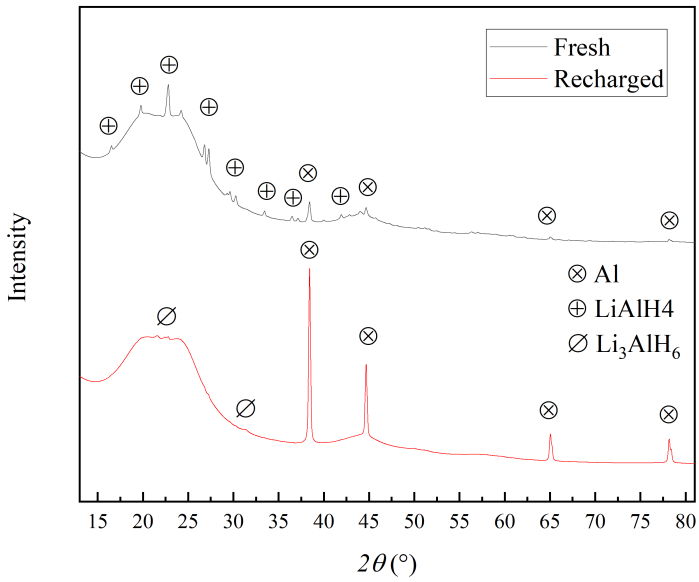

Figure 17. XRD results gathered for the 20 wt% sample, for the freshly synthesised sample and the sample on which a recharge procedure (180 bar of H_2 under 150 ℃, reached by a ramp rate of 10 ℃/min, 48h) was attempted.

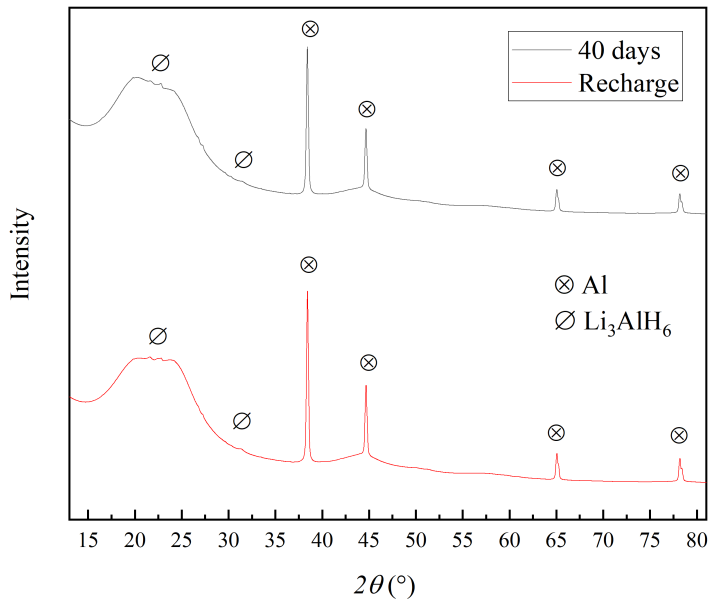

Figure 18. XRD results gathered for the 20 wt% sample, for the sample that spent 40 days in storage and the sample on which a recharge procedure (180 bar of H_2 under 150 ℃ reached by a ramp rate of 10 ℃/min, 48h) was attempted.

3.4. Conclusion

Ball milling synthesis of lithium alanate and Vulcan XC72R has shown a composite system with lowered dehydroganation on-set temperatures compared to the bulk material. With lower wt% of $LiAlH_4$ composites, release of H_2 at room temperature was demonstrated, suggesting an intense amount of scaffolding interactions and destabilisation. Decomposition behaviour of these composites in time was investigated for different composites – it was noted that in all cases a equilibrium state is reached. Higher wt% of $LiAlH_4$ retain higher efficiencies of release of H_2 after reaching the aforementioned equilibrum state. Another conclusion could be that lower wt% composites reach their equilibrium state faster than their higher wt% counterparts. This however requires more detailed investigation but presents a possibility of creating a model that precisely describes the processes that lead to this equilibrium state. This could be extrapolated to provide a more detailed kinetic description of these systems.

A recharge procedure was attempted, but no significant results were achieved. Additives in the form of transition metals might be considered as a supplement to the Vulcan XC72R in the hopes of achieving this. Other carbon blacks with modified surface parameters (including various activated, chemically modified surfaces) present another possibility of research, as well. However, one should keep in mind the practicallity of these solutions and the viability of their potential real-world application.

SUMMARY

$LiAlH_4$/Vulcan XC72R composites were synthesised using the ball milling method in various compositions – from 20 wt% $LiAlH_4$ to 80 wt% $LiAlH_4$, in increments of 10 wt%. The impact of different ball milling conditions was investigated in a series of samples (with 40 wt% composite). These composites were then characterised using temperature-programmed dehydrogenation, gas sorption, and X-ray diffraction. The behaviour of these composite systems was investigated after spending periods of time in storage. A recharge procedure was attempted, but was not successful.

The goal of this study was to investigate the impact of Vulcan XC72R on the dehydrogenation properties of $LiAlH_4$. The effect of time spent in storage was supposed to be impactful on their dehydrogenation properties and release efficiencies and it was investigated.

The results of the study showed that the effect of ball milling and the carbon scaffold is significant – a degree of confinement and strong interactions between the alanate and carbon scaffold could be deduced from the collected data. The systems show release of hydrogen at lower temperatures than bulk material – the lower the $LiAlH_4$ content, the lower the dehydrogenation on-set temperature e.g. the 20 wt% sample beginning to release H_2 from a temperature as low as 25 °C, reaching a peak of the first reaction step release at 71 °C. Systems of low enough wt% content of the alanate exhibit dehydrogenation that starts at room temperature and peaks at temperatures required for the use in PEM fuel cells (< 80 °C). Additionally, the effect of time spent in storage showed that an equilibrium level is reached and the H_2 release efficiencies afterwards remain stable, without apparent further decomposition. However, a more detailed and possibly mathematically modelled approach could be useful in the future.

Rehydrogenation attempts (180 bar of H_2 under 150 °C, 48h) failed, however. A further investigation is required into whether a recovery of hydrogen capacity of the systems and under what conditions that might be achievable. From available literature, a conclusion can be drawn that a way to lower the equilibrium pressure of the alanate system must be reached for this to be successful. It is then optimal to first determine whether interactions with the carbon scaffolding and confinement lower it at all. From there, it would become clear whether pursuing such a solution (i.e. combining lithium alanate with carbon black) is a viable option or an alternative one should be posited.

REFERENCES

[1] Arias, P. A., N. Bellouin, E. Coppolaet al.. (2021). Technical Summary. In: Climate Change 2021: The Physical Science Basis. Contribution of Working Group I to the Sixth Assessment Report of the Intergovernmental Panel on Climate Change [Masson-Delmotte, et al. (eds.)]. Cambridge University Press. In Press.

[2] Ogden, J. M. (1999). Prospects for building a hydrogen energy infrastructure. Annual Review of Energy and the Environment, 24(1), 227–279.

[3] Liu, K., Song, C., & Subramani, V. (Eds.). (2009). Hydrogen and Syngas Production and Purification Technologies.

[4] Howarth, R. W., & Jacobson, M. Z. (2021). How green is blue hydrogen? Energy Science & Engineering.

[5] Yusaf, T.; Laimon, M.; Alrefae, W.; Kadirgama, K.; Dhahad, H.A.; Ramasamy, D.; Kamarulzaman, M.K.; Yousif, B. Hydrogen Energy Demand Growth Prediction and Assessment (2021–2050) Using a System Thinking and System Dynamics Approach. Appl. Sci. 2022, 12, 781.

[6] Astiaso Garcia, D., Barbanera, F., Cumo, F., Di Matteo, U., & Nastasi, B. (2016). Expert Opinion Analysis on Renewable Hydrogen Storage Systems Potential in Europe. Energies, 9(11), 963.

[7] https://www.nationalgrid.com/stories/energy-explained/hydrogen-colour-spectrum; as accessed on 23.5.2022.

[8] Bérubé, V., Radtke, G., Dresselhaus, M., & Chen, G. (2007). Size effects on the hydrogen storage properties of nanostructured metal hydrides: A review. International Journal of Energy Research, 31(6-7), 637–663.

[9] S.A. Sherif, Frano Barbir, T.N. Veziroglu. (2005). Towards a Hydrogen Economy, The Electricity Journal, Volume 18, Issue 6, Pages 62-76, ISSN 1040-6190,

[10] https://www.energy.gov/eere/fuelcells/doe-technical-targets-onboard-hydrogen-storage-light-duty-vehicles, as accessed on 2.2.2022.

[11] https://cordis.europa.eu/programme/id/FP7, as accessed on 2.2.2022.

[12] Suárez-Alcántara, Tena-Garcia, & Guerrero-Ortiz. (2019). Alanates, a Comprehensive Review. Materials, 12(17), 2724.

[13] Mohtadi, R., & Orimo, S. (2016). The renaissance of hydrides as energy materials. Nature Reviews Materials, 2(3).

[14] DOE Hydrogen and Fuel Cells Program Record. Record #: 9013. (2009.) Energy requirements for hydrogen gas compression and liquefaction as related to vehicle storage needs

[15] Chen, P., Akiba, E., Orimo, S., Zuettel, A., & Schlapbach, L. (2016). Hydrogen Storage by Reversible Metal Hydride Formation. Hydrogen Science and Engineering : Materials, Processes, Systems and Technology, 763–790.

[16] N.A.A. Rusman, M. Dahari. (2016). A review on the current progress of metal hydrides material for solid-state hydrogen storage applications, International Journal of Hydrogen Energy, Volume 41, Issue 28, Pages 12108-12126.

[17] Jiang, Y., He, Y., & Liu, C. T. (2018). Review of porous intermetallic compounds by reactive synthesis of elemental powders. Intermetallics, 93, 217–226.

[18] Matar, S. F. (2010). Intermetallic hydrides: A review with ab initio aspects. Progress in Solid State Chemistry, 38(1-4), 1–37.

[19] Gupta, M., & Crivello, J. C. (2005). Hydrogen Storage Intermetallic Compounds: First Principles Investigations of Properties Relevant to Applications. Materials Science Forum, 475-479, 2489–2496.

[20] Møller, K., Sheppard, D., Ravnsbæk, D., Buckley, C., Akiba, E., Li, H.-W., & Jensen, T. (2017). Complex Metal Hydrides for Hydrogen, Thermal and Electrochemical Energy Storage. Energies, 10(10), 1645.

[21] Krishna, Rahul. (2012). Hydrogen Storage for Energy Application. Hydrogen Storage. Chapter: Hydrogen Storage for Energy Application. Intech Open

[22] Schneemann, A., White, J. L., Kang, S., Jeong, S., Wan, L. F., Cho, E. S., … Stavila, V. (2018). Nanostructured Metal Hydrides for Hydrogen Storage. Chemical Reviews.

[23] Bogdanović, B., Schüth, F., & Felderhoff, M. (2004). Light metal hydrides and complex hydrides for hydrogen storage. Chem. Commun., (20), 2249–2258.

[24] Bogdanović, B., & Schwickardi, M. (1997). Ti-doped alkali metal aluminium hydrides as potential novel reversible hydrogen storage materials. Journal of Alloys and Compounds, 253-254, 1–9.

[25] Slattery, D.K., Michael, D.H.. Complex Hydrides for Hydrogen Storage - Final Report. US Department of Energy Archives

[26] Nielsen, T. K., Besenbacher, F., & Jensen, T. R. (2011). Nanoconfined hydrides for energy storage. Nanoscale, 3(5), 2086

[27] Løvvik, O. M., Opalka, S. M., Brinks, H. W., & Hauback, B. C. (2004). Crystal structure and thermodynamic stability of the lithium alanates $LiAlH_4$ and Li_3AlH_6. Physical Review B, 69(13).

[28] Varin, R. A., & Zbroniec, L. (2010). Decomposition behavior of unmilled and ball milled lithium alanate ($LiAlH_4$) including long-term storage and moisture effects. Journal of Alloys and Compounds, 504(1), 89–101.

[29] Ares, J. R., Aguey-Zinsou, K.-F., Porcu, M., Sykes, J. M., Dornheim, M., Klassen, T., & Bormann, R. (2008). Thermal and mechanically activated decomposition of $LiAlH_4$. Materials Research Bulletin, 43(5), 1263–1275.

[30] Brinks, H. W., Hauback, B. C., Norby, P., & Fjellvåg, H. (2003). The decomposition of $LiAlD_4$ studied by in-situ X-ray and neutron diffraction. Journal of Alloys and Compounds, 351(1-2), 222–227.

[31] Fallas, J. C., Chien, W.-M., Chandra, D., Kamisetty, V. K., Emmons, E. D., Covington, A. M., Hagemann, H. (2010). Raman Spectroscopy Measurements of the Pressure−Temperature Behavior of $LiAlH_4$. The Journal of Physical Chemistry C, 114(27), 11991–11997.

[32] Ke, X., & Chen, C. (2007). Thermodynamic functions and pressure-temperature phase diagram of lithium alanates by *ab initio* calculations. Physical Review B, 76(2).

[33] Graetz, J. (2012). Metastable Metal Hydrides for Hydrogen Storage. ISRN Materials Science, 2012, 1–18.

[34] Chung, S.-C., & Morioka, H. (2004). Thermochemistry and crystal structures of lithium, sodium and potassium alanates as determined by ab initio simulations. Journal of Alloys and Compounds, 372(1-2), 92–96.

[35] Tomiyasu, K., Sato, T., Horigane, K., Orimo, S., & Yamada, K. (2012). Hydrogen release from Li alanates originates in molecular lattice instability emerging at ∼100 K. Applied Physics Letters, 100(19), 193901.

[36] Jang, J.-W., Shim, J.-H., Cho, Y. W., & Lee, B.-J. (2006). Thermodynamic calculation of $LiH \leftrightarrow Li_3AlH_6 \leftrightarrow LiAlH_4$ reactions. Journal of Alloys and Compounds, 420(1-2), 286–290.

[37] Wang, J., Ebner, A. D., & Ritter, J. A. (2006). Physiochemical Pathway for Cyclic Dehydrogenation and Rehydrogenation of $LiAlH_4$. Journal of the American Chemical Society, 128(17), 5949–5954.

[38] Eigen, N., Keller, C., Dornheim, M., Klassen, T., & Bormann, R. (2007). Industrial production of light metal hydrides for hydrogen storage. Scripta Materialia, 56(10), 847–851.

[39] Hauback, B. ., Brinks, H. ., & Fjellvåg, H. (2002). Accurate structure of $LiAlD_4$ studied by combined powder neutron and X-ray diffraction. Journal of Alloys and Compounds, 346(1-2), 184–189.

[40] Ashby, E. C., Brendel, G. J., & Redman, H. E. (1963). Direct Synthesis of Complex Metal Hydrides. Inorganic Chemistry, 2(3), 499–504.

[41] Chen, J., Kuriyama, N., Xu, Q., Takeshita, H. T., & Sakai, T. (2001). Reversible Hydrogen Storage via Titanium-Catalyzed $LiAlH_4$ and Li_3AlH_6. The Journal of Physical Chemistry B, 105(45), 11214–11220.

[42] Graetz, J., Wegrzyn, J., & Reilly, J. J. (2008). Regeneration of Lithium Aluminum Hydride. Journal of the American Chemical Society, 130(52), 17790–17794.

[43] Liu, X., Langmi, H. W., Beattie, S. D., Azenwi, F. F., McGrady, G. S., & Jensen, C. M. (2011). Ti-Doped $LiAlH_4$ for Hydrogen Storage: Synthesis, Catalyst Loading and Cycling Performance. Journal of the American Chemical Society, 133(39), 15593–15597.

[44] Humphries, T. D., Birkmire, D., McGrady, G. S., Hauback, B. C., & Jensen, C. M. (2017). Regeneration of $LiAlH_4$ at sub-ambient temperatures studied by multinuclear NMR spectroscopy. Journal of Alloys and Compounds, 723, 1150–1154.

[45] Zhao, L., Xu, F., Zhang, C., Wang, Z., Ju, H., Gao, X., … Liu, Z. (2021). Enhanced hydrogen storage of alanates: Recent progress and future perspectives. Progress in Natural Science: Materials International, 31(2), 165–179.

[46] Pundt, A., & Kirchheim, R. (2006). HYDROGEN IN METALS: Microstructural Aspects. Annual Review of Materials Research, 36(1), 555–608.

[47] Cao, G. (2004). NANOSTRUCTURES AND NANOMATERIALS Synthesis, Properties, and Applications. Imperial College Press.

[48] Hahn, H. (1997). Gas phase synthesis of nanocrystalline materials. Nanostructured Materials, 9(1-8), 3–12.

[49] Wang, H., Qiao, X., Chen, J., & Ding, S. (2005). Preparation of silver nanoparticles by chemical reduction method. Colloids and Surfaces A: Physicochemical and Engineering Aspects, 256(2-3), 111–115.

[50] Wahab, M. A., & Beltramini, J. N. (2014). Catalytic nanoconfinement effect of in-situ synthesized Ni-containing mesoporous carbon scaffold (Ni-MCS) on the hydrogen storage properties of $LiAlH_4$. International Journal of Hydrogen Energy, 39(32), 18280–18290.

[51] Chen, R., Wang, X., Xu, L., Chen, L., Li, S., & Chen, C. (2010). An investigation on the reaction mechanism of $LiAlH_4$–MgH_2 hydrogen storage system. Materials Chemistry and Physics, 124(1), 83–87.

[52] Xia, G., Meng, Q., Guo, Z., Gu, Q., Liu, H., Liu, Z., & Yu, X. (2013). Nanoconfinement significantly improves the thermodynamics and kinetics of co-infiltrated $2LiBH_4$–$LiAlH_4$ composites: Stable reversibility of hydrogen absorption/resorption. Acta Materialia, 61(18), 6882–6893.

[53] Toth, P. (2021). Nanostructure quantification of turbostratic carbon by HRTEM image analysis: State of the art, biases, sensitivity and best practices. Carbon, 178, 688–707.

[54] Lázaro, M.J. & Calvillo, Laura & Celorrio, Veronica & Pardo, Juan & Perathoner, Siglinda & Moliner, Rafael. (2011). Study and application of Vulcan XC-72 in low temperature fuel cells.

[55] M. Thommes, K. Kaneko, A.V. Neimark, J.P. Olivier, F. Rodriguez-Reinoso, J. Rouquerol, K.S.W. Sing, Physisorption of gases, with special reference to the evaluation of surface area and pore size distribution (IUPAC Technical Report), Pure Appl. Chem. 87 (2015) 1051–1069

[56] S. Pérez-Rodrígueza, E. Pastorb, M.J. Lázaroa. Electrochemical behavior of the carbon black Vulcan XC-72R: influence of the surface chemistry

[57] Sopicka-lizer, M. (2010). Introduction to mechanochemical processing. High-Energy Ball Milling, 1–5.

[58] Takacs, L., & McHenry, J. S. (2006). Temperature of the milling balls in shaker and planetary mills. Journal of Materials Science, 41(16), 5246–5249.

[59] Varin, R. A., & Zbroniec, L. (2012). Mechanical and Thermal Dehydrogenation of Lithium Alanate ($LiAlH_4$) and Lithium Amide ($LiNH_2$) Hydride Composites. Crystals, 2(2), 159–175.

[60] AutoChem 2950 HP Automated Catalyst Characterization System Operator's Manual, Micromeritics (2011).

[61] AutoChem II 2920 Brochure, Micromeritics (2017).

[62] Rzepka, M., Lamp, P., & de la Casa-Lillo, M. A. (1998). Physisorption of Hydrogen on Microporous Carbon and Carbon Nanotubes. The Journal of Physical Chemistry B, 102(52), 10894–10898.

[63] P.S. Liu, G.F. Chen. 2014. Characterisation methods:Basic Factors. Porous Materials Processing and Applications. 1st Ed. Butterworth-Heinemann

[64] Andrei A. Bunaciu, Elena gabriela Udriştioiu & Hassan Y. Aboul-Enein (2015) X-Ray Diffraction: Instrumentation and Applications, Critical Reviews in Analytical Chemistry, 45:4, 289-299

[65] Skoog, D.A.; Holler, F.J.; Crouch, S.R. Principles of Instrumental Analysis. Sixth Edition, Thomson Brooks/Cole, USA (2007).

[66] Guinebretière, R. (2007). X-ray diffraction by polycrystalline materials. Iste Ltd.

[67] iSorb HP series High Pressure Gas Sorption System Operating Manual, Quantachrome, (2019)

[68] Voigt, W. (1889). Ueber die Beziehung zwischen den beiden Elasticitätsconstanten isotroper Körper. Annalen Der Physik, 274(12), 573–587.

[69] Tuul, K. (2021). Ball-milled $NaAlH_4$/carbon black composites for reversible hydrogen storage. University of Tartu.

[70] Baizar, D., & Ledbetter, H. (1994). Accurate Modeling of Size and Strain Broadening in the Rietveld Refinement: The "Double-Voigt" Approach. Advances in X-Ray Analysis, 38, 397–404.

ACKNOWLEDGMENTS

This work was supported by the EU through the European Regional Development Fund under project TK141 2014-2020.4.01.15-0011 and Estonian Research Council grant PRG676.

Before all else, I would like to express my sincere gratitude to Dr. Rasmus Palm and Kenneth Tuul for their acceptance of me into the work group, their crucial help during my research and general support during my stay at the University of Tartu. This thesis is as much a result of their work as it is of mine.

Similar sentiment could be extended to the people that work in the Laboratory of Physical Chemistry, spearheaded by Prof. Enn Lust. The opportunity that was given to me to complete my Master's degree at the University of Tartu I do not take lightly, least of all when it was spent in such a healthy work environment as is the Laboratory of Physical Chemistry. Additionally, I would like to extend my thanks to Mr. Jaan Aruväli for his help on the XRD measurements.

Finally, a quick thank you (and love you!) is due to all the people that most definitely are not the inferno, but that do give me space, make me endure.

SUPPLEMENTARY INFORMATION

Supplementary section 1 – adsorption isotherms

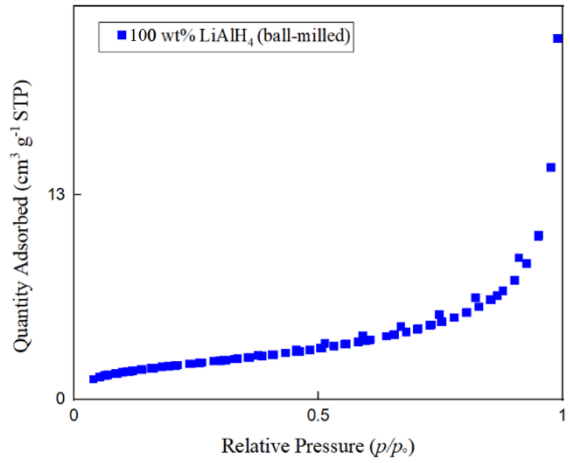

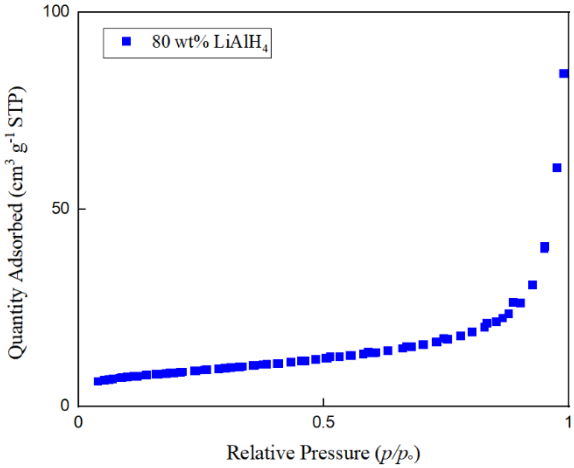

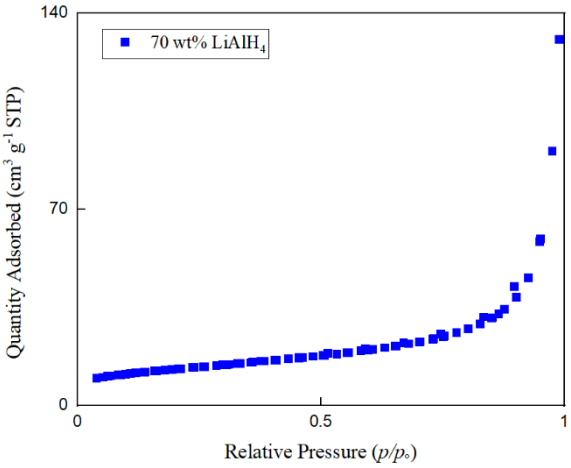

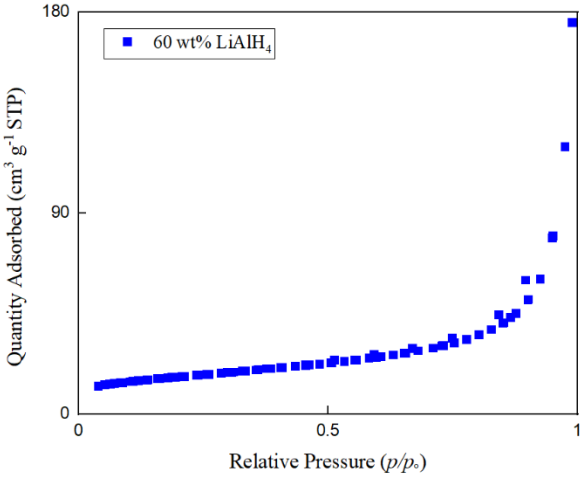

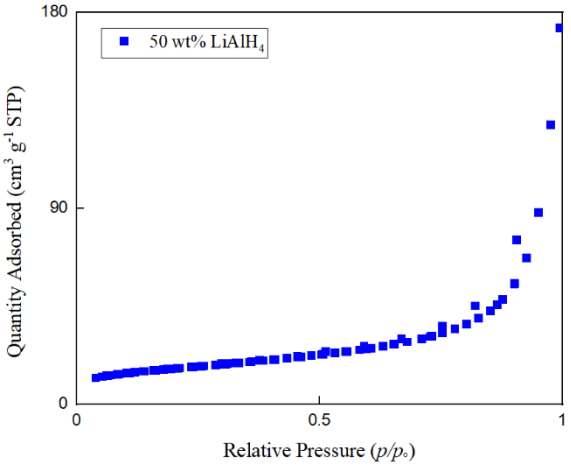

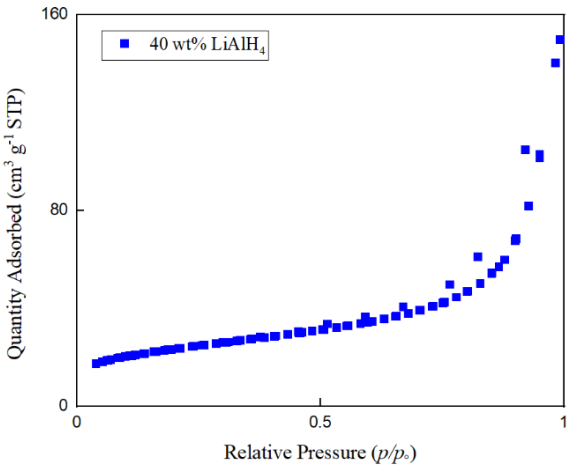

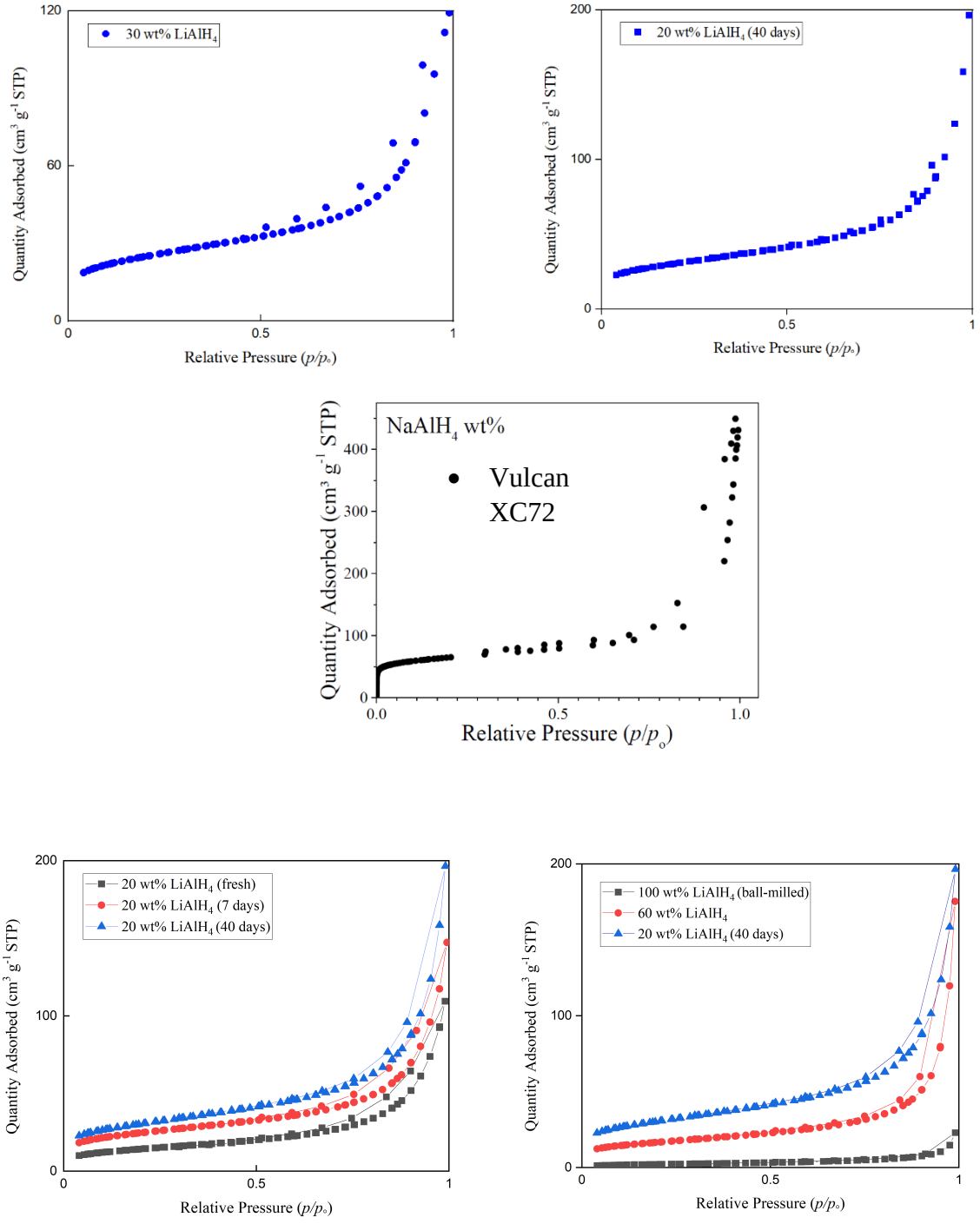

Supplementary figure 1. Gas adsorption isotherms for ball-milled lithium alanate, Vulcan XC72R[13], and different wt% composites.

[13] Data for Vulcan XC72R reused with permission from Mr. Kenneth Tuul [69]

Supplementary section 2 – X-ray diffraction refinement example

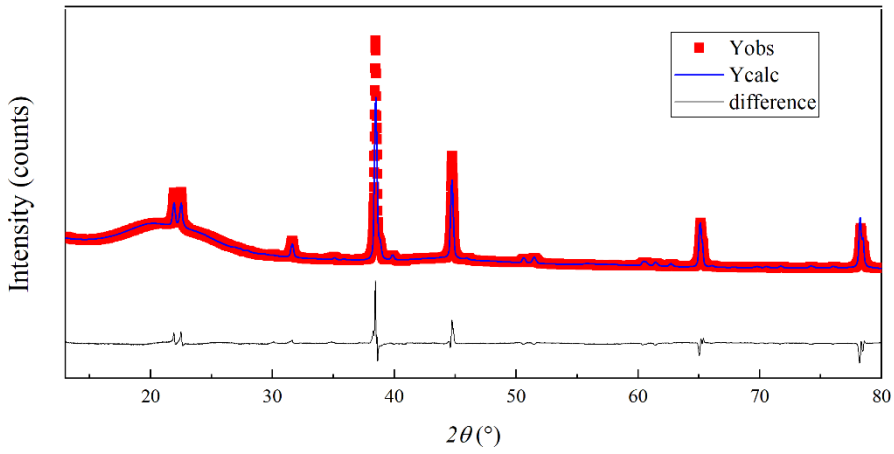

Supplementary figure 2. An example of the Rietveld refinement (which itself is based on the method of least squares of regression analysis) of the raw measurement data is presented. Yobs presents the experimentally observed data, Ycalc the calculated refined pattern, and difference presents the difference between the two. Presented on the 50 wt% $LiAlH_4$ composite. Difference was shifted by a flat factor of -40000 to allow for simultaneous plotting.

Non-exclusive licence to reproduce thesis and make thesis public

I, Pavle Ramah

1. herewith grant the University of Tartu a free permit (non-exclusive licence) to:

1.1. reproduce, for the purpose of preservation, including for adding to the DSpace digital archives until the expiry of the term of copyright, and

1.2 make available to the public via the web environment of the University of Tartu, including via the DSpace digital archives, under the Creative Commons licence CC BY NC ND 3.0, which allows, by giving appropriate credit to the author, to reproduce, distribute the work and communicate it to the public, and prohibits the creation of derivative works and any commercial use of the work from **07/06/2024** until the expiry of the term of copyright,

“Synthesis, characterisation, and analysis of the time degradation of lithium alanate/carbon black composites”

supervised by Dr. Rasmus Palm, and Kenneth Tuul (MSc.).

2.I am aware of the fact that the author retains the rights specified in p. 1.

3. I certify that granting the non-exclusive licence does not infringe other persons’ intellectual property rights or rights arising from the personal data protection legislation.

Pavle Ramah
31/05/2022